



Supplementary Materials for

Cassini finds molecular hydrogen in the Enceladus plume: Evidence for hydrothermal processes

J. Hunter Waite,* Christopher R. Glein,* Rebecca S. Perryman, Ben D. Teolis, Brian A. Magee, Greg Miller, Jacob Grimes, Mark E. Perry, Kelly E. Miller, Alexis Bouquet, Jonathan I. Lunine, Tim Brockwell, Scott J. Bolton

*Corresponding author. Email: hwaite@swri.edu (J.H.W.); cglein@swri.edu (C.R.G.)

Published 14 April 2017, *Science* **356**, 155 (2017)

DOI: 10.1126/science.aai8703

This PDF file includes:

Materials and Methods

Supplementary Text

Figs. S1 to S12

Tables S1 to S11

References

See also:

Simulation, modeling, and calibration codes and data products at <https://inms-support.space.swri.edu>

Materials and Methods

1. Analysis of INMS background in the E21 flyby data

1.1. Instrumentation

During a flyby, neutral gas enters both the closed and open source regions of the INMS instrument (Fig. S1). In the closed source (CS) inlet, the ambient gas enters and impacts the CS antechamber as a molecular beam at the ram speed. In the antechamber, the gas is isotropized, thermalized, and transmitted to the CS ionization region, and then ionized if the CS filament is turned on. In the open source (OS), the molecular beam traverses the source without impacting the internal ionizer surfaces. If the OS filament is turned on, the molecular beam is partially ionized in the OS ionization volume (the volume occupied by the filament electrons). The ions are guided by a series of ion optics that reject thermally ionized gases through biasing of the ion fore optics, and select the desired mass and velocity combination using a quadrupole switching lens. During the E21 flyby, the velocity filter values were selected to scan the range of velocity distributions of the gas.

The quadrupole switching lens can be set to analyze either the open or closed source ion beam, and can switch between OSNB and CSN operating modes as commanded every 2.314 seconds. There are additional ion optical elements downstream of the quadrupole switching lens that direct gas into the quadrupole mass analyzer: a mass filter that transmits the selected mass ions to the channel electron multiplier (CEM) where data are acquired.

1.2. Determination of background sources

The INMS mass 2 OSNB signal observed in Enceladus' plume is produced from H₂ present in the plume as well as a background signal that must be subtracted. We investigate a number of background sources, including: i) dissociative ionization of the H₂O beam in the OS forming H₂⁺ (section 1.2.1); ii) ion leakage of H₂⁺ ions generated from neutral H₂ and H₂O in the CS (section 1.2.2); iii) background from thermalized H₂ and H₂O in the instrument (section 1.2.2); and iv) radiation (section 1.2.3). We estimated expected background signals using results from laboratory measurements on the INMS Refurbished Engineering Unit (REU), together with the CSN and OSNB signals acquired during the E21 flyby.

1.2.1. Dissociative ionization of the water beam in the open source

Electron impact ionization of H₂O creates ions with excess internal energy, resulting in dissociation (fragmentation) of the molecule to create smaller ions. For H₂O the fragments include OH⁺, H⁺, and H₂⁺, while for the deuterium isotopologue of water, HDO, the dissociation products include OD⁺, D⁺, and D₂⁺. Both H₂⁺ and D⁺ from dissociative ionization of the water molecular beam in the OS contribute to the background signal at mass 2. The fragments are produced in the OS ionization region with the 8.5 km s⁻¹ velocity of the molecular beam, plus any excess translational kinetic

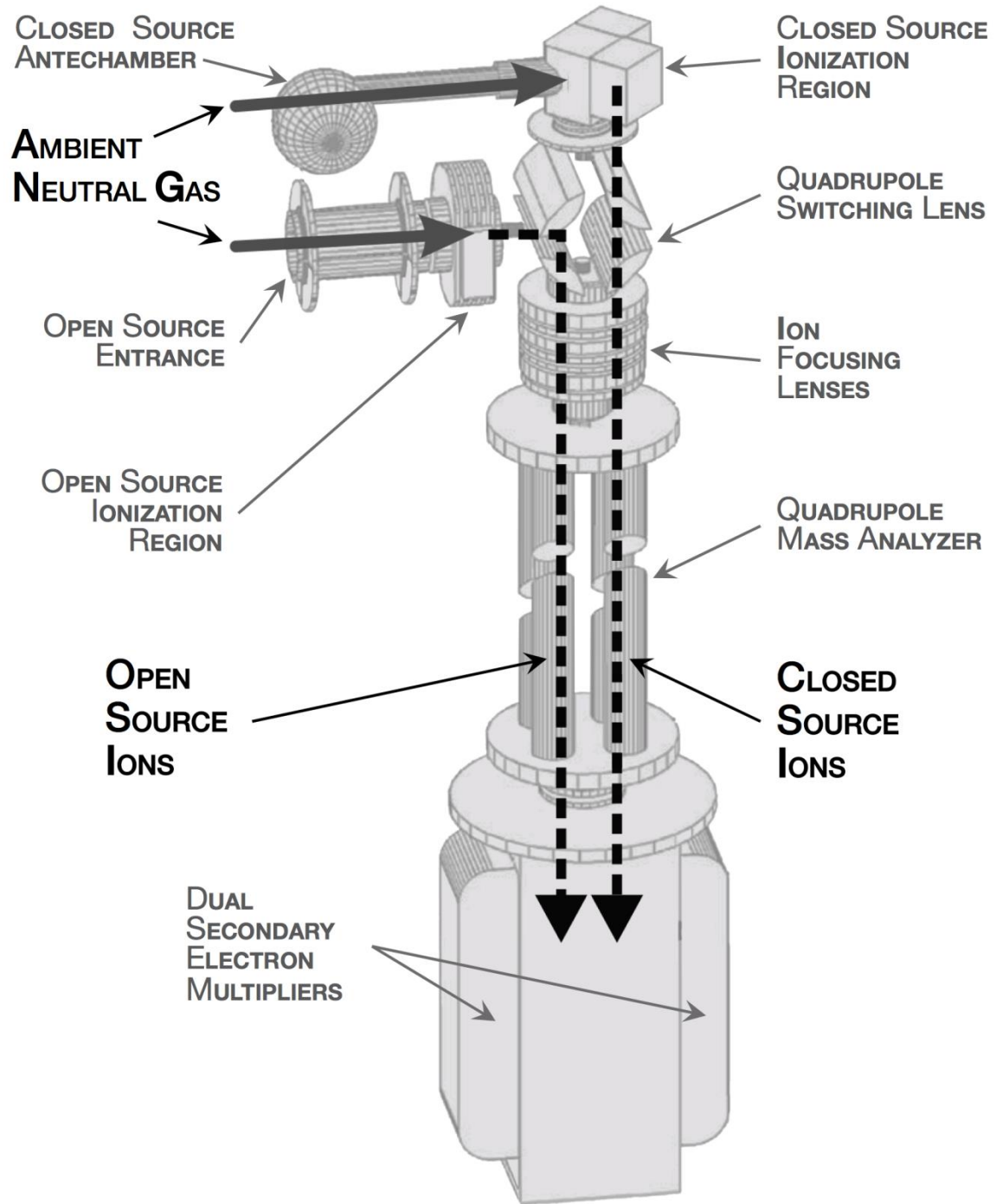


Fig. S1. Diagram of the INMS instrument. INMS has inlets for gases into closed and open ion sources (solid arrows). The dashed arrows indicate the subsequent paths of the ions created by ionization in the closed or open sources.

energy from the dissociative ionization process. However, published data on the H_2^+ energy distribution from H_2O electron impact dissociative ionization may not exist. We therefore considered two limiting cases: i) ‘cold’ H_2^+ with <0.1 eV excess energy which (to good approximation) retains the 8.5 km s^{-1} (0.75 eV for H_2) forward-directed beam velocity; and ii) ‘hot’ H_2^+ with several eV or more (much faster than 8.5 km s^{-1}), and therefore approximately isotropic in the INMS frame of reference. Case i yields a larger estimated background signal than Case ii, since forward-directed ions have a greater probability of transmission through the instrument. We consider both cases below, including the additional minor contribution of D^+ fragments to the signal. The signal obtained from Case i is used as a conservative estimate for the contribution from dissociative ionization to the total background signal, which is subsequently used in the estimation of the $\text{H}_2/\text{H}_2\text{O}$ ratio in the plume.

1.2.1.1. ‘Cold’ H_2^+

‘Cold’ H_2^+ ions (Case i above) are created in the OS with approximately the same velocity distribution as the H_2O in the molecular beam. We therefore estimated the mass 2 background using the mass 18 OSNB signal of H_2O^+ from H_2O ionization, after applying factors for i) the relative cross sections for making H_2O^+ , H_2^+ , HDO^+ , and D^+ from electron impact of H_2O and HDO ; and ii) the ‘geometrical effect’, discussed further below and (more extensively) in section 2.3.

McConkey et al. (37) provide the latest review of dissociative ionization of water, including cross sections for all dissociative ionization processes as a function of electron energy. INMS ionizes material with 70 eV electrons. We examine the range of electron impact energies from 60 to 80 eV for H_2^+ relative to that of H_2O^+ . We find the following in Table 14 of (37): i) At 60 eV, $\text{H}_2^+/\text{H}_2\text{O}^+$ is 5.32×10^{-4} ; ii) at 70 eV, $\text{H}_2^+/\text{H}_2\text{O}^+$ is 5.43×10^{-4} ; and iii) at 80 eV, $\text{H}_2^+/\text{H}_2\text{O}^+$ is 4.81×10^{-4} . The spread in these values is smaller than the estimated laboratory uncertainty for the H_2^+ measurement of $\pm 16\%$. We adopt $(5.43 \pm 0.93) \times 10^{-4}$ for the ratio of $\text{H}_2^+/\text{H}_2\text{O}^+$.

We also include a small contribution to the mass 2 channel from D^+ produced by dissociative ionization of HDO with 70 eV electrons. The amount of D^+ produced can be expressed as $\text{D}^+/\text{H}_2\text{O}^+ = (\text{D}^+/\text{HDO}^+) \times (\text{HDO}^+/\text{H}_2\text{O}^+)$. The ratio of $(\text{D}^+/\text{HDO}^+) = 0.110 \pm 0.007$, which accounts for D^+ production from HDO being half that of H^+ from H_2O (37). The ratio $(\text{HDO}^+/\text{H}_2\text{O}^+) = (6 \pm 2) \times 10^{-4}$ can be obtained from the previously reported D/H ratio (19). Using these values, we calculate $\text{D}^+/\text{H}_2\text{O}^+ = (0.66 \pm 0.22) \times 10^{-4}$. This can be compared to H_2^+ production from H_2O , which gives $\text{H}_2^+/\text{H}_2\text{O}^+ = (5.43 \pm 0.93) \times 10^{-4}$ (37). Therefore, the relative contributions to mass 2 from this source of background are $\sim 89\%$ from H_2^+ and $\sim 11\%$ from D^+ leading to a total ratio of $(6.1 \pm 0.9) \times 10^{-4}$.

The velocity scans adjust the OSNB ion transmission relative to both the position on the surface of Enceladus and the velocity distribution of the outflowing gas. The H_2^+ formed from dissociative ionization has the same velocity distribution as the H_2O^+ , but the OSNB transmission differs between the two as a function of energy and position within the ion source region. Therefore, a ‘geometric’ factor is applied to correct for the lower OSNB transmission of mass 2 relative to mass 18 in the part of the gas velocity space that corresponds to molecules arriving from the direction of the Enceladus tiger

stripes (owing to the wider velocity bandpass at mass 2 than at mass 18; see sections 2.2 and 2.3).

On the basis of the INMS ray tracing and Enceladus plume modeling discussed in section 2, we estimated that the geometric factor increased during the velocity scans in a sawtooth fashion as the scans repeated from ~ 0.015 to ~ 0.65 ($\pm 50\%$) relative to the signal of counts obtained by interpolating between the maxima in the OSNB mass 18 signal during the scans (Fig. S2; see section 2.2 for the estimation of the OS sensitivity function from ray tracing, and section 2.3 for further discussion of the mass 18 behavior during the velocity filter scans).

Accordingly, we estimated the H_2^+ background by i) interpolating between the mass 18 OSNB maxima as shown in Fig. S2; ii) applying the combined $(\text{H}_2^+ + \text{D}^+)/\text{H}_2\text{O}^+$ dissociative ionization ratio of $(6.1 \pm 0.9) \times 10^{-4}$; and iii) scaling by the sawtooth geometric factor.

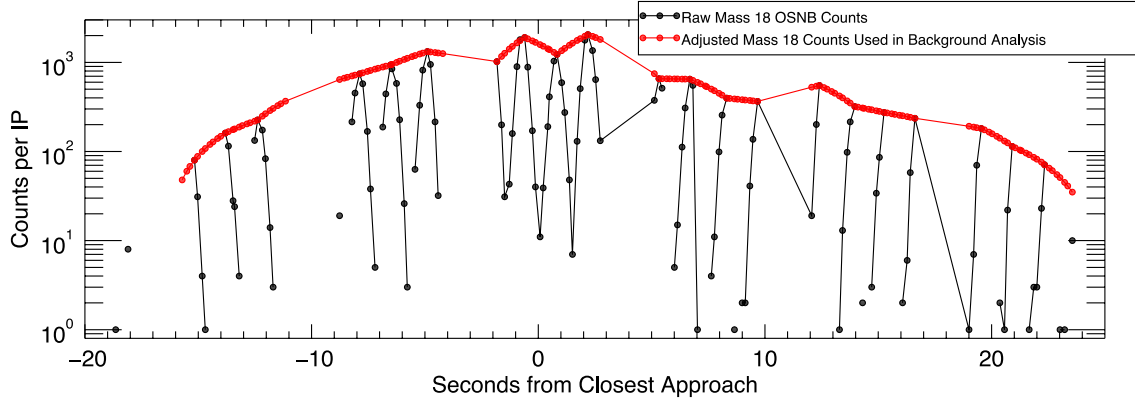


Fig. S2. Mass 18 OSNB raw and interpolated signal. Mass 18 (H_2O) counts observed during OSNB mode are shown in black. Velocity-scan-corrected mass 18 counts used in the background analysis are shown in red.

1.2.1.2. ‘Hot’ H_2^+

In the opposite limiting case of ‘hot’ H_2^+ generation from the molecular beam at several eV energies (much higher than the 8.5 km s^{-1} beam velocity), the ions have an approximately isotropic velocity distribution in the INMS reference frame. We therefore neglected the beam velocity in this case, and estimated the contribution of hot H_2^+ from dissociative ionization of the H_2O beam in the OS by taking into consideration only beam density, which is equal to the density of the ambient gas measured by the CS at mass 18 (Fig. S3). Following (21), the relationship between ambient density and CSN counts is

$$n_a = A \frac{1}{D_{CS}} \left(\frac{T_0}{T_a} \right)^{\frac{1}{2}} \frac{X_{m18}^{CSN}}{s}, \quad (\text{S1})$$

where n_a is the ambient gas density, D_{CS} is the CS ram factor, T_a and T_0 are the ambient gas temperature and room temperature, s is the species-dependent calibration sensitivity

[$2.87 \times 10^{-10} \text{ m}^3 \text{ s}^{-1}$, including the factor 1.55 sensitivity reduction discussed by (21)], and X_{m18}^{CSN} is the CSN count rate (counts per IP divided by the 0.031 sec integration time). The adsorption correction A was not included by (21), who restricted their analysis to volatile gases. Water adsorption in the instrument introduces a time distortion in the CSN mass 18 signal that lowers the measured peak density near closest approach, which we have corrected here by setting $A = 1.5 \pm 0.3$ [based on the results of (38)]. Additionally, the CSN measurements have coarser time resolution than the OSNB data, with CSN mass 18 counts measured only at -2.45 and +3.37 sec from closest approach, which is about 6 sec apart (Fig. S3). Accordingly, we approximated the time evolution of the H₂O density by interpolating the mass 18 maxima of the OSNB velocity scans (Fig. S2), and then scaling to the absolute density measured by the CS between -2.45 and +3.37 sec (Fig. S3). The proportionality factor between the H₂O density and the OSNB mass 2 signal due to water is the product of several factors

$$X_{m2+}^{OSNB} = \gamma \alpha I (\sigma_{H2+}^{H2O} + \kappa \sigma_{D+}^{HDO}) s n_a, \quad (\text{S2})$$

where $I = 1.88 \times 10^{14} \text{ electrons s}^{-1}$ is the OS filament emission flux (30 μA emission current), $\gamma \sim 0.1 \pm 0.03$ is an ionizer efficiency factor given by the fraction of the ionization volume intercepted by the molecular beam, and α is a transmission efficiency factor estimated from laboratory experiments (section 1.2.2.2) for H₂⁺ transmission from the filament ionization region to the detector, which includes the effect of the ion optics, velocity filter, and quadrupole mass filter.

The contribution to the mass 2 OSNB signal from D⁺ via dissociative ionization of HDO in the molecular beam is given by

$$(\sigma_{H2+}^{H2O} + \kappa \sigma_{D+}^{HDO}) / \sigma_{H2+}^{H2O} \sim 1.1 \quad (\text{S3})$$

where $\kappa = (6 \pm 2) \times 10^{-4}$ is the observed Enceladus plume HDO/H₂O ratio (19), and $\sigma_{D+}^{HDO} = 1.4 \times 10^{-17} \text{ cm}^2$ is the D⁺ production cross section from electron impact of HDO at 70 eV.

We estimated the factor $\gamma \sim 0.1$ from the ratio of the molecular beam 0.81 mm² cross section area (10.2 mm diameter) to the estimated OS ionization region, which is $9 \pm 3 \text{ mm}^2$ in total cross section area perpendicular to the beam (the product of the $2.9 \pm 0.9 \text{ mm}$ estimated filament slit length and the 3.1 mm OS ionizer depth).

Substituting Eq. S2 into Eq. S1, we obtain the relationship of the CSN H₂O⁺ signal to the mass 2 OSNB signal

$$X_{m2+}^{OSNB} = \frac{\gamma A \alpha I (\sigma_{H2+}^{H2O} + \kappa \sigma_{D+}^{HDO})}{D_{CS}} \left(\frac{T_0}{T_a} \right)^{\frac{1}{2}} X_{m18}^{CSN}. \quad (\text{S4})$$

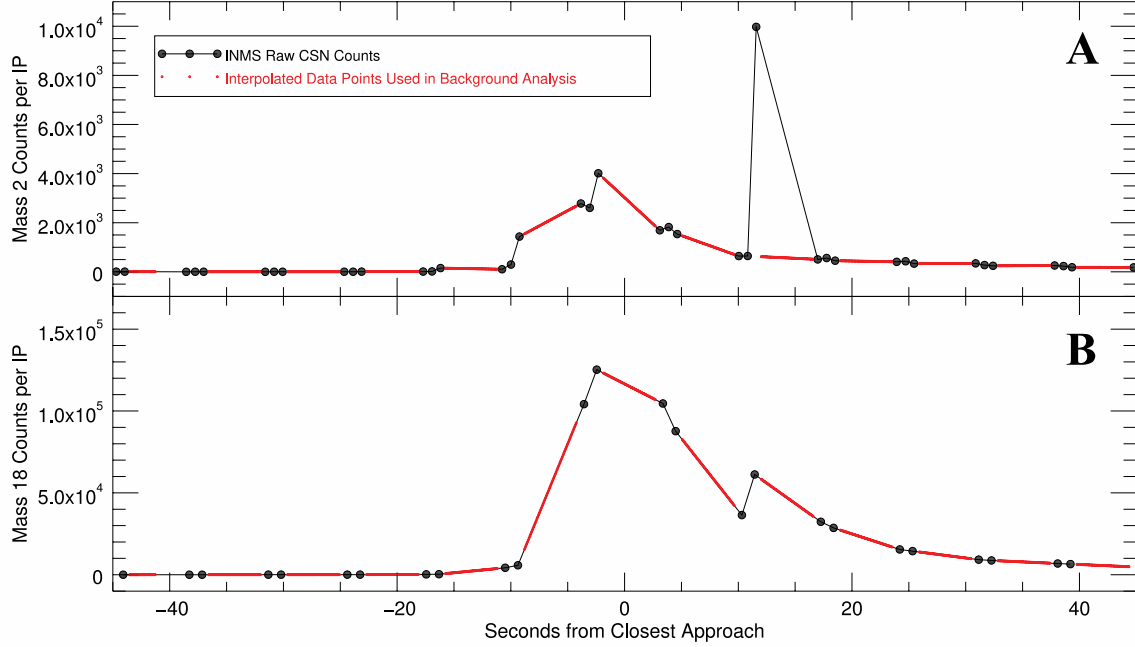


Fig. S3. Interpolated mass 2 and mass 18 spectra from the closed source. CSN data for mass 2 (A) and mass 18 (B) are shown as black points. INMS can only operate in one mode (CS or OS) at a time. To estimate the background during OSNB mode that could be caused by leakage from the CS, the CSN counts needed to be interpolated. With the exception of one H₂ data point (gray lines), all data were used in the interpolation (red lines). The single H₂ spike that was not used is characteristic of an ice grain in the CS, and the signal is expected to have returned to the reduced level by the time OSNB mode began operating again.

We eliminate the T_a dependence by noting that the product $D_{CS}\sqrt{T_a}$ is approximately independent of T_a in the limit of high (suprathermal) spacecraft speeds as at E21. Using the expressions of (21) (see their Eqs. A13-14 and C1-C3), we can write in the high-speed limit

$$D_{CS}\sqrt{T_a} \sim 0.7(2\pi m/k)^{1/2}u, \quad (\text{S5})$$

where u and m are the spacecraft speed and H₂O molecular mass, and the factor 0.7 corrects for thermalized gas leakage out of the instrument [this is the factor $R_0+R_2R_1$ from (21)]. Therefore, at the high E21 spacecraft speed (8.5 km s⁻¹) we can approximate Eq. S4 by

$$X_{m2+}^{OSNB} \sim \frac{\gamma A a l (\sigma_{H2+}^{H2O} + \kappa \sigma_{D+}^{HDO})}{1.4\sqrt{\pi}\delta} X_{m18}^{CSN}, \quad (\text{S6})$$

where $\delta = u/u_0$ is the ratio of the spacecraft speed u to the most probable speed $u_0 = \sqrt{2kT_0/m}$ of room-temperature gas molecules. With $u = 8500 \text{ m s}^{-1}$ and $u_0 = 519 \text{ m s}^{-1}$ for H_2O at room temperature, we have $\delta = 16.4$.

We calibrated the transmission efficiency α on the basis of laboratory experiments on the REU, described in section 1.2.2, in which the ratio of H_2O^+ CSN counts to those of H_2^+ in OSNB mode were measured at the E21 voltage settings during exposure of the INMS to thermal H_2O gas. In the laboratory, $T_a = T_0$ (the ambient gas is at room temperature), $D_{CS} = 1$ (no ram factor), $A = 1$ (no sticking correction; the H_2O exposure is long enough for water adsorption/desorption in the instrument to equilibrate), and $\gamma = 1$ (the thermal gas occupies the entire OS ionization volume). Inserting these values into Eq. S4, we solved for α_0 , which is the transmission efficiency under the conditions of the experiment during which ions are created in the OS from the entire ionization volume

$$\alpha_0 = \frac{(X_{m2+}^{OSNB} / X_{m18}^{CSN})}{I(\sigma_{H2+}^{H2O} + \kappa_0 \sigma_{D+}^{HDO})}, \quad (\text{S7})$$

where $\kappa_0 = 3.08 \times 10^{-4}$ is the $\text{HDO}/\text{H}_2\text{O}$ ratio of the experimental H_2O source. With the values of I , σ_{H2+}^{H2O} , and σ_{D+}^{HDO} given above, and the ratio $X_{m2+}^{OSNB} / X_{m18}^{CSN} = (8.1 \pm 0.4) \times 10^{-6}$ measured in the laboratory experiment (Table S1, section 1.2.2), Eq. S7 yields $\alpha_0 = (5.8 \pm 0.3) \times 10^3 \text{ s m}^{-2}$.

To estimate α (the in-flight transmission efficiency), we considered two limiting cases for the relationship of α to α_0 : i) thermal gas ionized outside the molecular beam ionization volume, i.e., away from the OS center axis, is not transmitted at all, such that $\alpha = \alpha_0 / \gamma \sim 10\alpha_0$; or ii) the thermal and molecular beam transmission factors are equal, i.e., $\alpha = \alpha_0$. This gives a range $5.8 \times 10^3 \leq \alpha \leq 5.8 \times 10^4$ for the in-flight transmission efficiency.

Accordingly, for the present case of ‘hot’ H_2^+ the predicted OSNB mass 2 counts from dissociative ionization of the water molecular beam in the OS has an order of magnitude uncertainty. From Eq. S6, we have

$$(3.4 \times 10^{-8}) X_{m18}^{CSN} \leq X_{m2+}^{OSNB} \leq (3.4 \times 10^{-7}) X_{m18}^{CSN}. \quad (\text{S8})$$

Therefore, even at the peak $1.25 \times 10^5 X_{m18}^{CSN}$ counts per IP near closest approach (Fig. S3), the estimated hot H_2^+ OSNB background from dissociative ionization of the H_2O beam is only 0.004 to 0.04 mass 2 counts per IP; i.e., one to two orders of magnitude below the estimated mass 2 counts for the ‘cold’ H_2^+ upper limiting case. The latter ‘conservative’ case is the one plotted in Fig. S4.

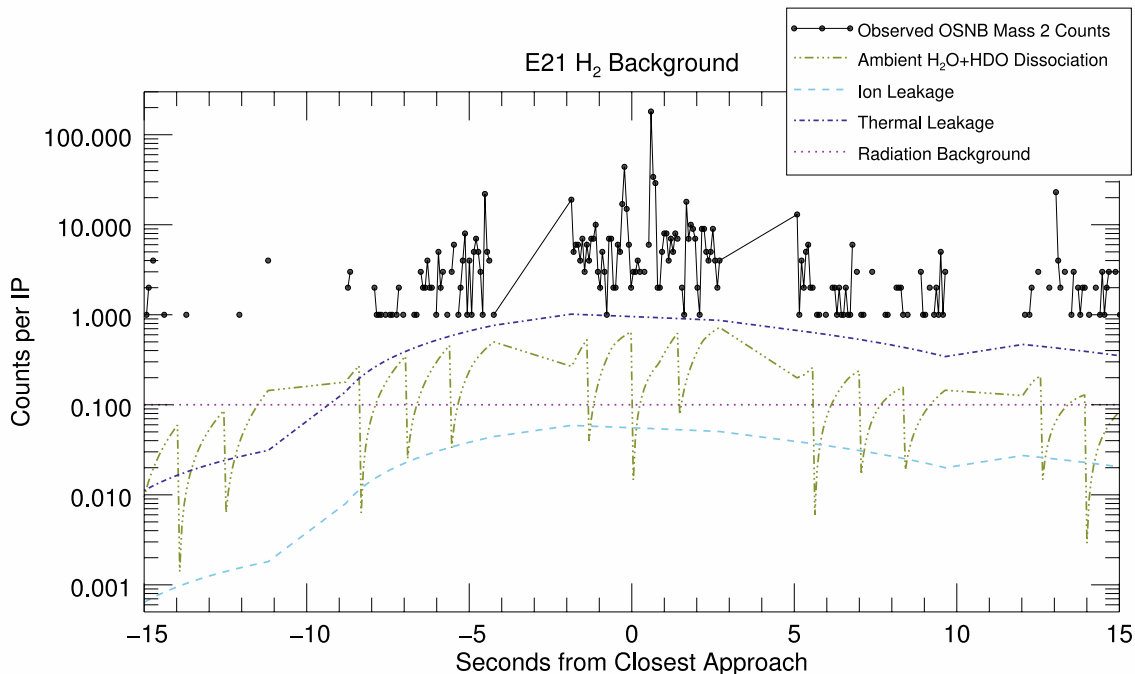


Fig. S4. Comparison of individual background sources to mass 2 signal. The expected counts per IP for the four sources of background during the E21 flyby are shown in comparison to the mass 2 OSNB signal in black. The summed background is displayed in Fig. 2.

1.2.2. Laboratory calibration experiments: Ion leakage and thermal background

Two additional types of background contribute to the mass 2 signal in Cassini INMS: ion leakage and thermal background. Ion leakage is the small portion of ionized gas from the CS that “leaks” through the electrostatic barrier of the quadrupole switching lens when it is set to measure H_2^+ in OSNB mode, and can originate from either electron impact on H_2 or dissociative ionization of H_2O in the CS. Thermal background refers to thermalized H_2 or H_2O background in the instrument that leaks into the OS ionization region [see (21) for an analysis of the gas conductances inside INMS]. Although the ion optics are designed to reject this thermal contribution, a small portion leaks through the quadrupole switching lens into the quadrupole analyzer. Both ion leakage and thermal background were quantified by making laboratory measurements using the INMS Refurbished Engineering Unit.

We base estimates for ion leakage and thermal background on modifications of the same basic experimental procedure. We warmed the filaments for ~ 12 hr to eliminate outgassing in the source, and configured the INMS REU optics to the flight settings of E21. The REU OSNB velocity compensation optics were configured to screen out thermal gas and admit only H_2 traveling at 8.5 km s^{-1} (0.75 eV). With the calibration chamber at base pressure, we recorded a series of background mass scans for both CSN and OSNB modes. Each scan covers mass-to-charge (m/z) ranges 1-8 and 12-23 and is comprised of integral mass “samples”, each of which has a 1000 ms integration period.

Following the background scans, we introduced a test gas mixture into the calibration chamber (20% H₂/noble gas mixture – for safety – in the H₂ experiments, and H₂O gas generated by a helium sparged water vapor inlet in the H₂O experiments), and stabilized the pressure at 1.2×10^{-7} Torr by regulating the flow of gas from the inlet manifold. We chose these conditions to simulate the CS gas density in flight. Preliminary calibration measurements with H₂O indicated that this density yields approximately the same number of mass 18 counts per IP as observed during the E21 flyby.

To quantify the ion leakage and thermal background within the instrument, we recorded a series of data sets consisting of 20 mass scans each by alternating the REU operating mode between CSN and OSNB with the unit programmed to switch modes at the start of each new data set. We configured the main sensor ion optics to nominal flight unit specifications for CSN, and set the OSNB mode velocity scan parameters (V_{cmp}) to correspond to E21 telemetry data to simulate instrument operations near closest approach (8.5 km s^{-1}). For each data set, we summed the ion counts for each mass across the scans and subtracted the background from the total counts. We calculated the leakage ratio as the average OSNB counts per sample divided by the average CSN counts per sample. We computed the statistical uncertainty of the parent population’s leakage ratio from the total counts for each mode in each experiment using a Poisson distribution. Details pertaining to the ion leakage and thermal background REU experiments are provided in sections 1.2.2.1 and 1.2.2.2, respectively.

Using the leakage ratios from the laboratory experiments (Table S1) and the correction factors for the thermal background (section 1.2.2.2), background signals from ion leakage and thermal background were calculated for the E21 flyby data. To determine the expected background signal from ion and thermal background of H₂ and H₂O, the corresponding leakage ratios were multiplied by the interpolated CSN counts (following the interpolation procedure described in section 1.2.1.2). The resulting expected background signals from ion and thermal leakage are plotted in Fig. S4.

Table S1. Summary of results from INMS REU. Laboratory experiments with the INMS REU were performed to determine the rates of ion and thermal leakage within the instrument. Figure S4 shows the resulting background signal for each source during the E21 flyby.

Background source (type of leakage)	Observation modes	Number of samples	Average counts	Ratio of OSNB:CSN	Ratio uncertainty
H ₂ ⁺ from thermal H ₂ background	OSNB – H ₂ CSN – H ₂	600 345	33.6 103934.8	3.24×10^{-4}	2.28×10^{-6}
H ₂ ⁺ ion leakage from H ₂	OSNB – H ₂ CSN – H ₂	160 160	0.05 94820.1	5.27×10^{-7}	1.86×10^{-7}
H ₂ ⁺ from thermal H ₂ O background	OSNB – H ₂ CSN – H ₂ O	320 320	1.23 161718.5	7.61×10^{-6}	3.95×10^{-7}
H ₂ ⁺ ion leakage from H ₂ O	OSNB – H ₂ CSN – H ₂ O	320 320	0.08 18654.8	4.63×10^{-7}	9.0×10^{-8}

1.2.2.1. Ion leakage

To measure the background signal from ion leakage out of the CS, we configured the REU with the OS filament off (such that gas in the OS was not ionized) and the CS filament on (generating ions in the CS ionization region). With the filaments in this arrangement, ions detected by the CEM detectors during testing can only have originated from the CS, since neutral gas in the OS was not ionized and thus cannot be transmitted through the instrument. To be detected, an ion must exit the CS, transit the switching-lens potential barrier, and arrive at the CEM detectors. By comparing the number of detected ions during CSN mode and those that were observed during OSNB mode, we obtained an estimate (Table S1) for the proportion of ions recorded during OSNB mode that actually originated from neutral gas ionized in the CS.

1.2.2.2. Thermal background

Thermal background is defined as the proportion of neutral thermal gas (ambient gas thermally equilibrated after entering the instrument through either the OS, CS, or INMS vent apertures) that contributes to the INMS signal while it is operating in OSNB mode. For these experiments, the sensor was configured with the OS filament on and the CS filament off. To be detected, neutral molecules must diffuse from other parts of the instrument into the OS ionization region. The results of these experiments include hydrogen molecules that enter through the OS and CS plus residual gas internal to the instrument. The detected ions can only originate from ionization in the OS, after which they are steered through the instrument by the quad switching lenses and counted by the CEM detectors.

In contrast to the laboratory experiments in which the gas densities in the OS and CS differed only by a source temperature factor $(T_{cs}/T_{os})^{1/2}$ (with the whole INMS immersed in thermal gas), the in-flight densities differ by $(T_{cs}/T_{os})^{1/2}(D_{os}/D_{cs})$ (with D the source ram factor) since ram flux arriving at the CS and OS competes with gas leakage out of the instrument to space (21). A correction to the laboratory CSN/OSNB ratios that takes into consideration the gas conductances and leakage paths through the instrument is therefore necessary to estimate the corresponding ratios in flight. There are two cases: i) H₂O thermal background resulting from water ram flux entering the instrument through the CS and OS; and ii) H₂ thermal background mostly produced by H₂O-Ti⁰ reactions from ice grain impacts in the CS gas inlet antechamber [(19); although the H₂ background also includes a smaller native H₂ component entering the antechamber, section 3.2].

For Case i, vapor (i.e., H₂O) entering the CS and OS, (21) gives a value of $D_{os}/D_{cs} = 2.1$ in the limit of high spacecraft speed and small ram angle as at E21. However, (21) applied a simplified approach to the analysis of the OS density that assumed that all gas entering the OS is thermalized by wall collisions and then escapes the OS with a low (0.17 mm²) effective area. This approach is acceptable for most INMS pointing directions [e.g., the T85, T88, and T96 Titan flybys analyzed by (21)], but overestimates the OS density at small ram angles (a few degrees or less) and high (suprathermal) ram speed. Under these conditions, the collimated molecular beam is transmitted completely through the OS without thermalizing wall collisions. To treat this

special case, we modified the model of (21) by negating the contribution of the molecular beam to the OS density. We did this by reducing the top plate aperture effective area A_{60} in their Eq. A.29a by 70%, which is the fraction of the incoming flux in the molecular beam according to Monte Carlo simulations (21). We ignored the negligible ($\sim 0.6\%$) fraction of the molecular beam flux that diffuses back into the OS after transiting the OS and thermalizing in the INMS Ion Source Enclosure. The modified calculation yields an estimated ratio of $D_{OS}/D_{CS} = 1.04 \pm 0.26$; that is, relative to the CS density, the in-flight OS thermal H₂O density is a factor 1.04 ± 0.26 times the laboratory OS density. We therefore apply a correction factor 1.04 ± 0.26 in converting the laboratory ratios of OS to CS H₂O counts to those expected in flight.

We approximated Case ii, vapor produced only in the CS (i.e., H₂), by negating all gas conduction pathways that convey gas into the instrument via the OS or the INMS vent [setting $A_{40} = A_{50} = A_{60} = 0$ in Eqs. A.10 of (21)], leaving leakage out of the CS as the only gas source through the instrument to the OS. In this special case [owing to the small conductance in/out of the OS relative to that of the vent; see Table 1 and Fig. 4 of (21)], the modified calculation gives $D_{OS}/D_{CS} = 0.033 \pm 0.008$; i.e., with respect to the CS H₂ density, the in-flight OS H₂ density is only a fraction 0.033 ± 0.008 of the laboratory OS density. Accordingly, we applied a factor 0.033 ± 0.008 in converting laboratory OSNB/CSN H₂ counts to those anticipated in flight.

1.2.3. Radiation

Based on analyses of past INMS data (39), radiation noise is expected to be approximately 0.1 counts per IP. This background source should also be removed from the E21 mass 2 OSNB signal, and is plotted in Fig. S4 along with the other background sources.

2. Using INMS ray tracing simulations and plume models to determine the H₂ to H₂O ratio from the E21 flyby

2.1. Introduction

The determination of the INMS OS response to the measured H₂ and H₂O gas densities during the E21 flyby requires: i) understanding the velocity phase space response of the instrument to the incoming gas; and ii) applying this response to the phase space distribution of the gas, which we have estimated from previous observations of the plume structure during flybys at altitudes near 75 km. In section 2.2, we review the ray tracing of the instrument response performed to understand the phase space response of the instrument. In section 2.3, we describe the plume modeling that is used to reproduce the E21 data set as closely as possible. In section 2.4, we derive the H₂/H₂O ratio based on the modeled results from section 2.3.

2.2. Ray tracing the open source response

Since H₂ at 8.5 km s^{-1} enters the OS at an energy of only 0.75 eV, which is too low to easily reproduce in the calibration laboratory, we determined the dependence of the

INMS OS sensitivity function on molecular mass and velocity using the ion optics software simulator SIMION (40). An understanding of this dependence allows modeling of the INMS OS in its E21 operational configuration. These simulations of the charged particle trajectories were then verified and validated against laboratory measurements for molecular nitrogen at higher energies.

We modeled the entire traversal of the ions through the instrument, from the OS entrance aperture where they start as neutrals, through the ionizer and the quadrupole switching lens (QL for quad lens; Fig. S1), and then through the quadrupole mass analyzer [including ion transmission through the time dependent radio frequency (RF) field in the analyzer]. Since the E21 velocity filter scans were performed by adjusting the QL voltages as a function of time, we performed multiple SIMION simulations each with different QL voltage settings corresponding to the instrument configuration for a particular velocity compensation value (V_{cmp}). Simulations were performed to correspond to each of the V_{cmp} values in the velocity filter scans around closest approach (each unique QL configuration used in flight within ± 3 seconds of E21 closest approach was simulated) to capture the evolution of the sensitivity function during the scans, as described below.

The INMS OS and quadrupole mass sensor cross-section is shown in Fig. S5A. This figure shows the major ion optical components modeled by SIMION. The entry angle definitions and cylindrical coordinate system are shown as they were modeled. These coordinates were later converted to the spacecraft frame of reference. The model was constructed using the available dimensions for the ion source, transfer optics, and quadrupole mass filter to create a full three-dimensional, finite difference model using SIMION's solid geometry language. The finite difference model was built using four independent sections (each with a density of 0.08 mm/grid unit) that were assembled by carefully matching the boundary conditions at the interfaces of the sections. The first section treats the open ion/neutral source, entrance deflectors, top plate aperture, ionization region, and transfer optics. These elements are arranged in front of the QL and are used to multiplex the two open and closed ion sources shown in Fig. S5B. The second section consists of the QL (velocity filter) and its housing. The third section is a construction of the exit transfer optics including the split plates and exit nozzle. The fourth section consists of the BS (beam shaping) lens and the quadrupole mass filter, which is comprised of a set of four hyperbolic rods and a detector plane.

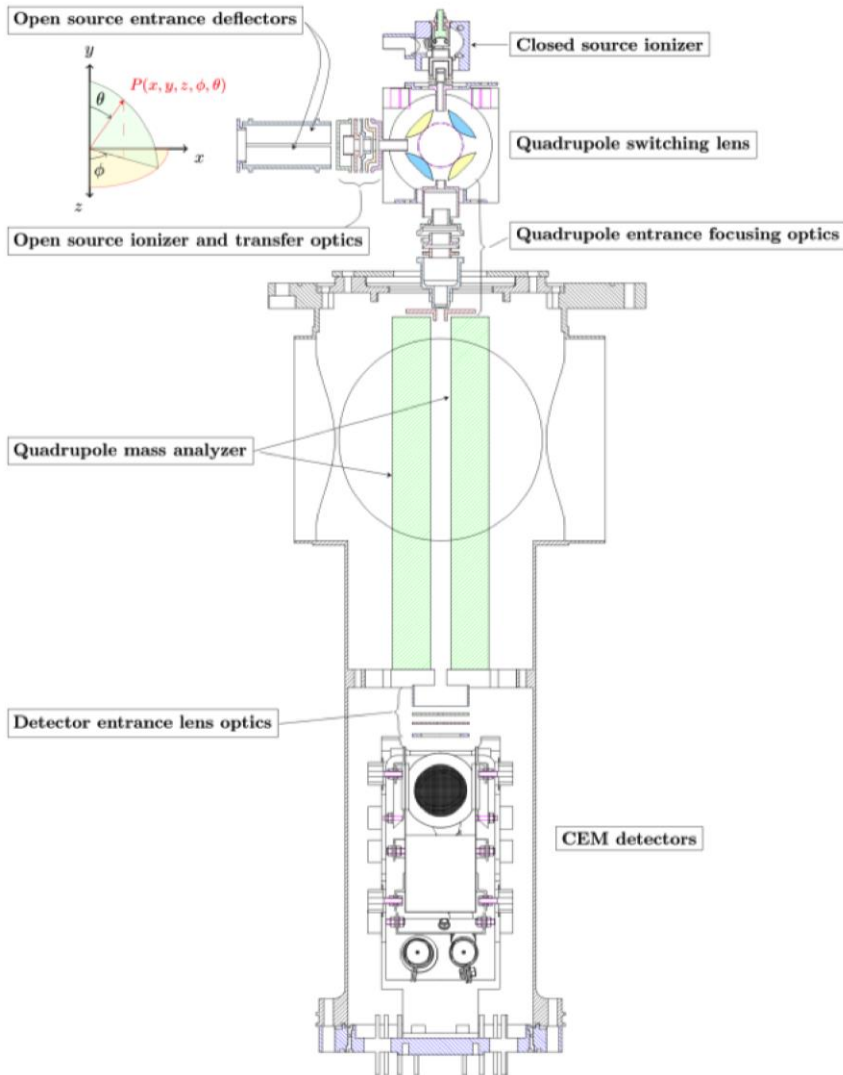
A

Fig. S5. Diagram of INMS optics. A: An overview of the optics for both the CS and OS in Cassini INMS.

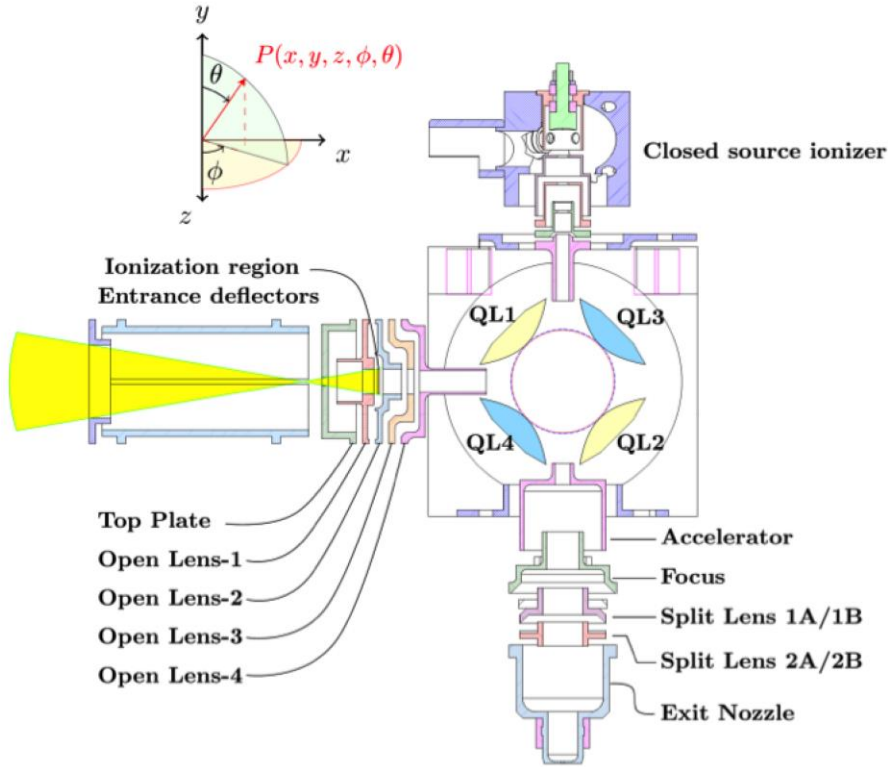
B

Fig. S5 (Cont'd). Diagram of INMS optics. B: Zoomed-in image of Cassini INMS OS and transfer optics. The transmitted distribution of neutrals is shown in yellow.

The model electrode potentials were defined and adjusted via a custom program written in Mathematica using the SIMION command line interface (available upon request due to ITAR restrictions), while the dynamics of the quadrupole mass analyzer, RF frequency, RF and direct current (DC) voltage amplitude, phase and quadrupole DC offset were calculated using a custom-written Lua code (included in other Supplementary Materials). Mass selection was performed by varying the RF potential to satisfy the relation

$$m/z \approx \frac{0.55 \times (Urf)}{f^2}, \quad (S9)$$

where m/z is given in u, Urf represents the RF peak-to-peak amplitude in volts, and f stands for the frequency of the RF in MHz. The mass analyzer quadrupole rod set in Cassini INMS operates at two RF frequencies: 3.57 MHz for 1 to 8 u, and 1.64 MHz for 12 to 99 u. These values were verified using measurements performed on the laboratory REU. We performed computational experiments by reading the E21 voltage settings directly into the simulation program, which assigned static and dynamic voltages to the SIMION model. Ion and neutral Monte Carlo particle distributions were generated by the software and loaded into SIMION, and then ray traced through the optics.

To simulate ionization of neutral particles beaming into the INMS OS in OSNB mode, a flat (uniform) neutral particle distribution in energy and angle is first generated

to ensure that the angular acceptance space of the INMS analyzer is filled. After passing through the outer and inner apertures (top lens apertures in Fig. S5B), the transmitted distribution of neutrals is collected at the ionization region of the open ion source. This distribution of neutral particles entering the ionization region represents the minimum and maximum angular acceptance beaming into the ionization region through the apertures. The simulation code then changes the distribution of neutral particles to ions by switching the charge state to +1. This new ion distribution, which has an initial set of entry position, velocity, and direction parameters, is traced through the rest of the INMS optics using the E21 OS voltage parameters. To realistically model the quadrupole mass filter transmission, the simulation program scrambles the ion time-of-birth between 0 and f^{-1} . This scrambling ensures that the ions do not all arrive at the same phase of the RF during the simulation.

Figure S6 shows an example simulation of INMS operation in OSNB mode. The ion starting position is the ionization volume of the OS. Two ion populations are simulated: H_2^+ and H^+ . The mass analyzer RF/DC was set to transmit $m/z = 2$ u, simulating H_2^+ ions. It can be seen that $m/z = 1$ u is quickly filtered out near the front of the quadrupole rod set while transmitting H_2^+ ions to the detector. In Figs. S7 and S8, we show the OS sensitivity function for low-energy H_2 during the E21 velocity filter scan for a single QL voltage generated by matching the digital-to-analog converter (DAC) settings to the OSNB mode settings used in flight for E21. Figure S7 shows the sensitivity as a function of azimuth (φ) and elevation angle (θ) for a single DAC setting of the QL voltage scan, where we have integrated over φ and θ . In Fig. S8, we integrate over θ to highlight the energy dependence of the sensitivity function. The energy distribution appears bimodal due to the poor DAC resolution at the low energy range of the QL used on INMS. In neutral mode operation, OS focusing lenses 1 and 2 (OL1, OL2) are programmed to discriminate between gas particles that have thermally accommodated to the ion source walls and the direct beaming components at spacecraft energies. When gas particles are ionized at spacecraft thermal energies, the potential barrier set up between OL1 and OL2 lens elements rejects transmission and focusing of these ions into the analyzer. In the simulation, these values are set to the same potential as the flight unit, and we observe a sharp cut-off for particle energies below this threshold.

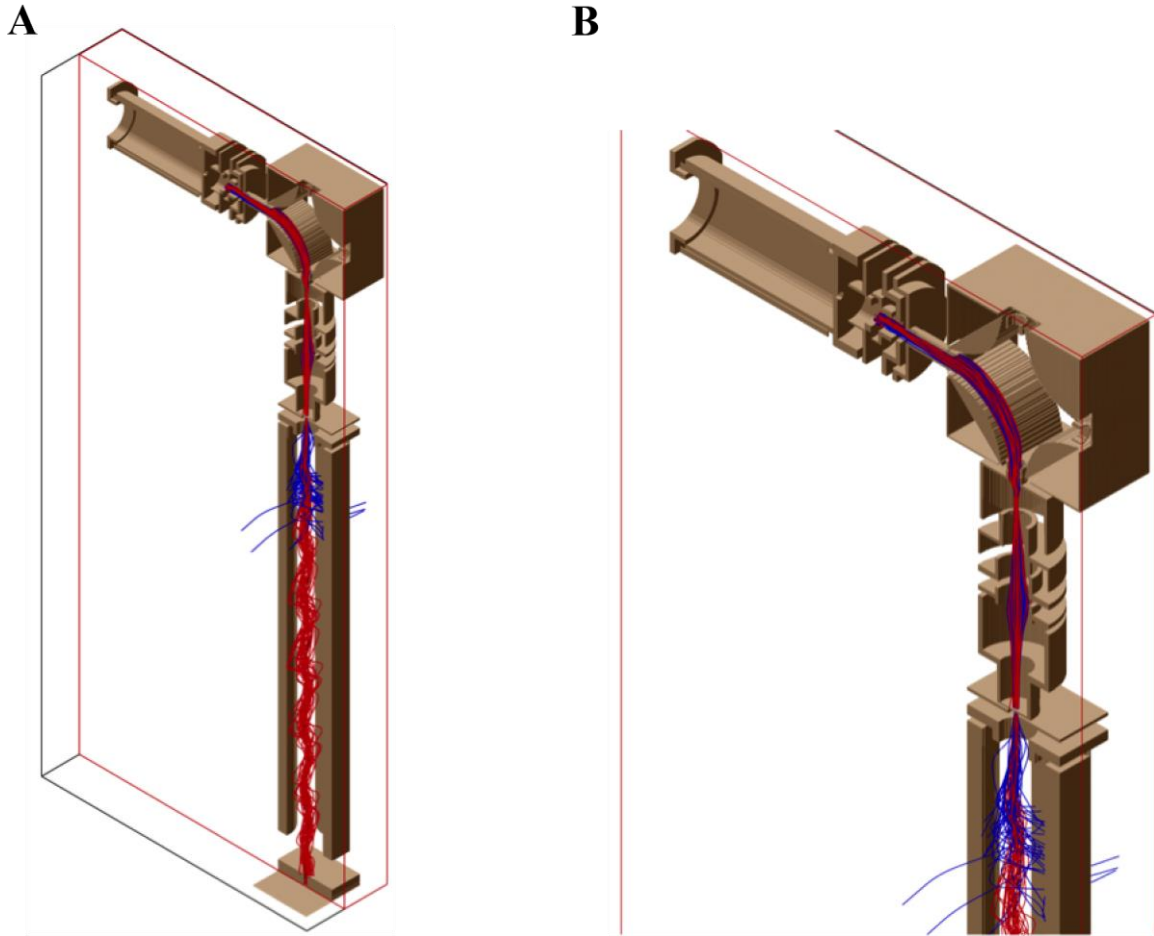


Fig. S6. Simulations of H₂⁺ and H⁺ transmission in OSNB mode. A: Cut-away view of the INMS SIMION simulations for H₂⁺ (red) and H⁺ (blue) transmission run with a 3.67 MHz RF frequency, with the RF/DC ratio optimized to transmit H₂⁺ ions. B: Zoomed-in view of panel A.

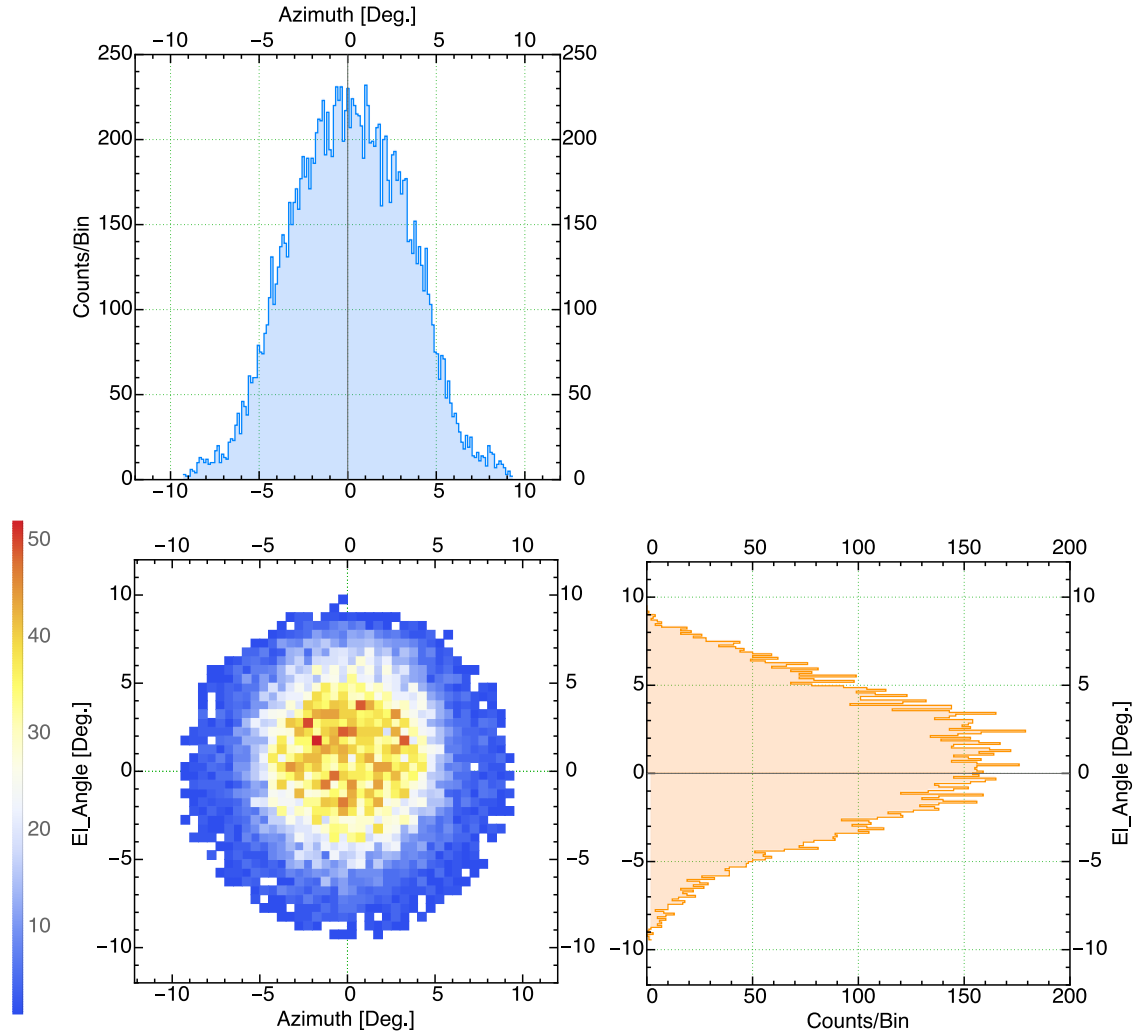


Fig. S7. Response of OS sensitivity to azimuth and elevation angle. Simulated cross-sections of the azimuth-elevation angular response for H₂ using OSNB E21 parameters for a single QL switching lens voltage, which is set by DAC values used on E21. The color bar gives binned counts.

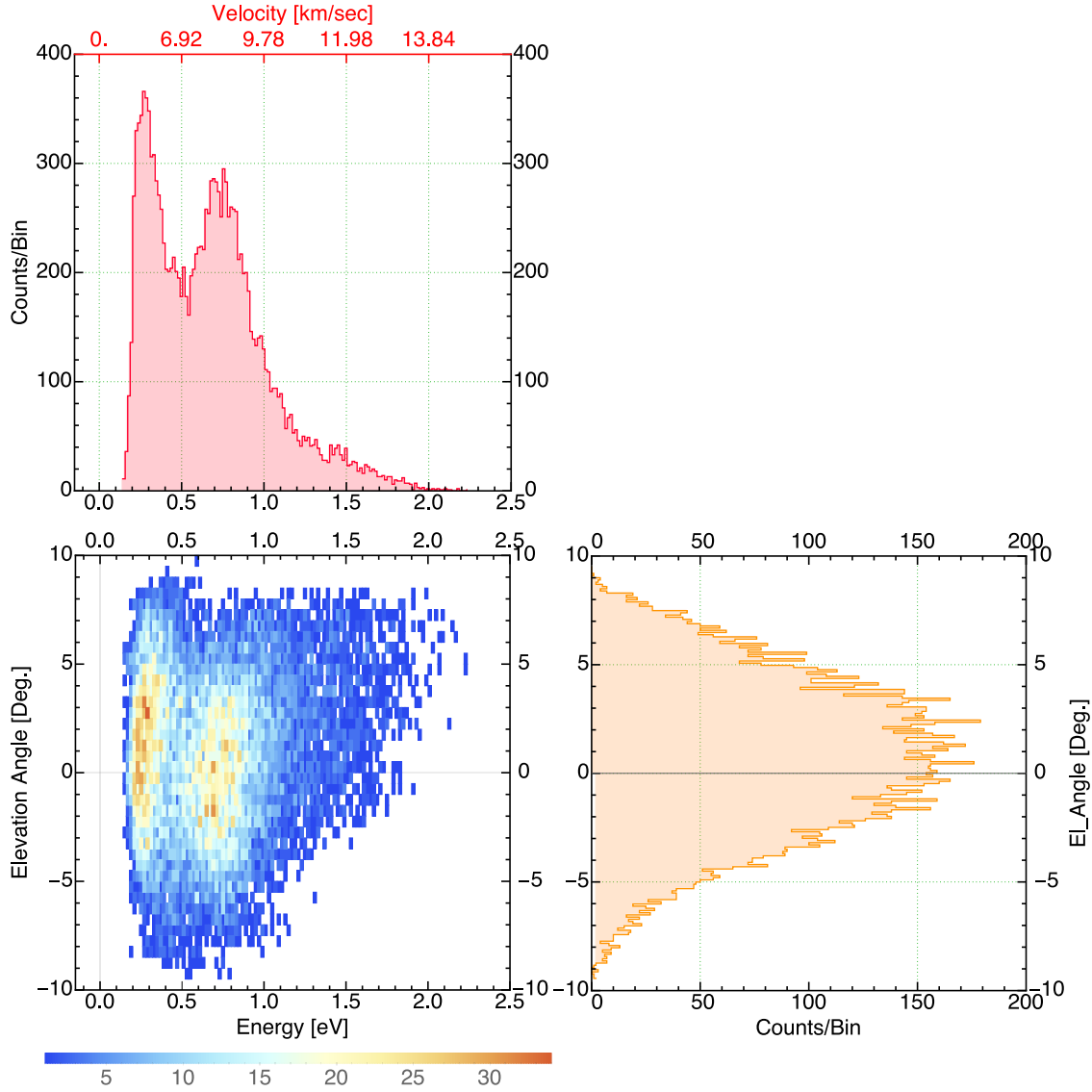


Fig. S8. Response of OS sensitivity to energy and elevation angle. Simulated H_2^+ elevation angle (θ) response as a function of energy illustrating the energy dependence of the sensitivity function. The color bar gives binned counts. This figure along with Fig. S7 define the complete energy-angle response of the sensitivity.

2.3. Modeling E21 plume outflow

We estimated the OSNB sensitivity to the plume gas by comparing the OS sensitivity function from the ray tracing simulations (Figs. S7 and S8; section 2.2) to an outflow model of the plume density spatial and velocity distribution using MATLAB (included in other Supplementary Materials). The model was fit to i) Cassini Ultraviolet Imaging Spectrograph (UVIS) measurements of the plume H_2O column density (24); and to ii) INMS measurements of the CO_2 density, as measured in CSN mode along the trajectories of the low-altitude E14 (99 km altitude), E17 (74 km altitude), and E18 (74

km altitude) flybys. For INMS, CO₂ was modeled since it does not stick to the instrument walls and therefore tracks the plume density more accurately than H₂O (38).

We modeled the plume source as either uniformly distributed along the tiger stripes, or as consisting of multiple jets with source locations and jet pointing directions as estimated from imaging (41). We approximated the jet velocity distribution as a sum of drifted Maxwellians (simulating a distribution of gas bulk velocity). The Maxwellian approach allows the gas density and velocity distributions to be approximated by an analytical function of distance from the plume source and angle from the jet center axis (42), enabling computationally fast iterations through the plume parameter space which consists of source locations, rates, Mach numbers, and jet pointing directions. These parameters were optimized to match i) the modeled gas distribution with the observed CO₂ distributions along the individual INMS flyby trajectories; and ii) the modeled column density profile with the H₂O distributions observed along the occultation line of sight from each of the individual UVIS occultations. Assuming as an approximation that all gas species are ejected from the plume with equilibrated temperatures and bulk velocities, we extrapolated the density and velocity distributions of different species, including H₂, with lighter species having a greater thermal velocity spread.

The OS sensitivity function gives the distribution of velocities accepted and detected by the instrument, which we translated into the Enceladus velocity reference frame and mapped onto Enceladus' surface by approximating the molecular paths as straight lines (hence neglecting gravity and intermolecular collisions), and considering the source locations along the tiger stripes (Fig. S9). Using the source rate, bulk velocity, and Cassini's position relative to the source location and jet center axis, we estimated the signal from each source. By summing the signals from all modeled sources, we estimated the total OS signal versus time, taking into consideration the change of the OS sensitivity function during the velocity filter scans as well as the spacecraft ram angle, velocity, and position versus time.

The predicted and observed responses of the H₂O signal to the velocity filter scans are in approximate agreement (Fig. S10); the model predicts both the approximate shape and amplitude of the peaks and their correspondence with the velocity filter scans. The maxima in H₂O observed near closest approach on each scan can be understood by translating the velocity filter scans, which are programmed to increase monotonically, into Enceladus' reference frame by adding the spacecraft velocity vector. In the Enceladus frame, the velocities accepted by the OS do not increase monotonically over the course of a single 1.3 sec scan. Instead, the accepted velocities first decline, reach a minimum, and then increase. These minima are approximately coincident with the peaks of H₂O signal (Fig. S10), indicating that INMS is scanning the downward sloping, high speed tail of the H₂O velocity distribution. This effect is also partly due to the projection (near minimum V_{gas}) of the OS sensitivity function to the jet sources closest to (i.e., directly below) Cassini.

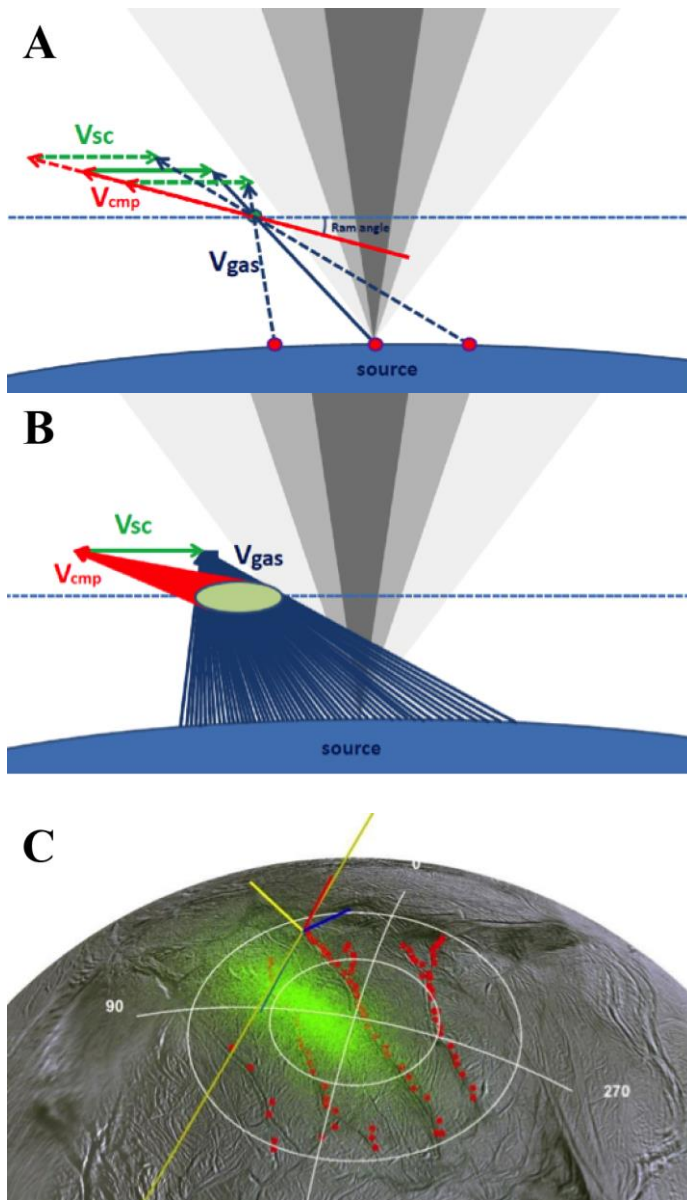


Fig. S9. Mapping of the gas source. A: Diagram showing the effect of the velocity filter scans and the translation of the OS velocity filter setting into the Enceladus reference frame by vector addition of the spacecraft velocity. The velocity filter is set to accept the velocity vector labeled V_{cmp} (solid red arrow) tilted by a 3° ram angle (exaggerated in the diagram) to the spacecraft velocity vector (labeled V_{sc} ; solid green arrow). The difference between V_{cmp} and V_{sc} yields the velocity vector, V_{gas} (solid blue arrow) in the Enceladus reference frame. The dashed arrows show the effect of the velocity filter scans on the vector addition. It can be seen that the scans shift both the magnitude of the V_{gas} vector accepted by the OS and the surface location to which the vector projects.

B: Diagram showing the effect of the wide velocity bandpass (in velocity space) of the OS sensitivity function (represented in the diagram by the gray oval). The OS in reality accepts a wide range of velocities below and above the velocity filter setting, which project to a continuum of Enceladus surface locations.

C: Projection (green smudge) of the OS sensitivity function (H_2O shown) from the ray tracing (Figs. S7 and S8) onto Enceladus' surface. Red dots denote the tiger stripe sources from (41), the yellow line traces the E21 trajectory (with Cassini moving toward the bottom of the diagram), and the red, yellow, and blue axes are the spacecraft x , y , and z coordinate system (drawn from Cassini's position in the diagram).

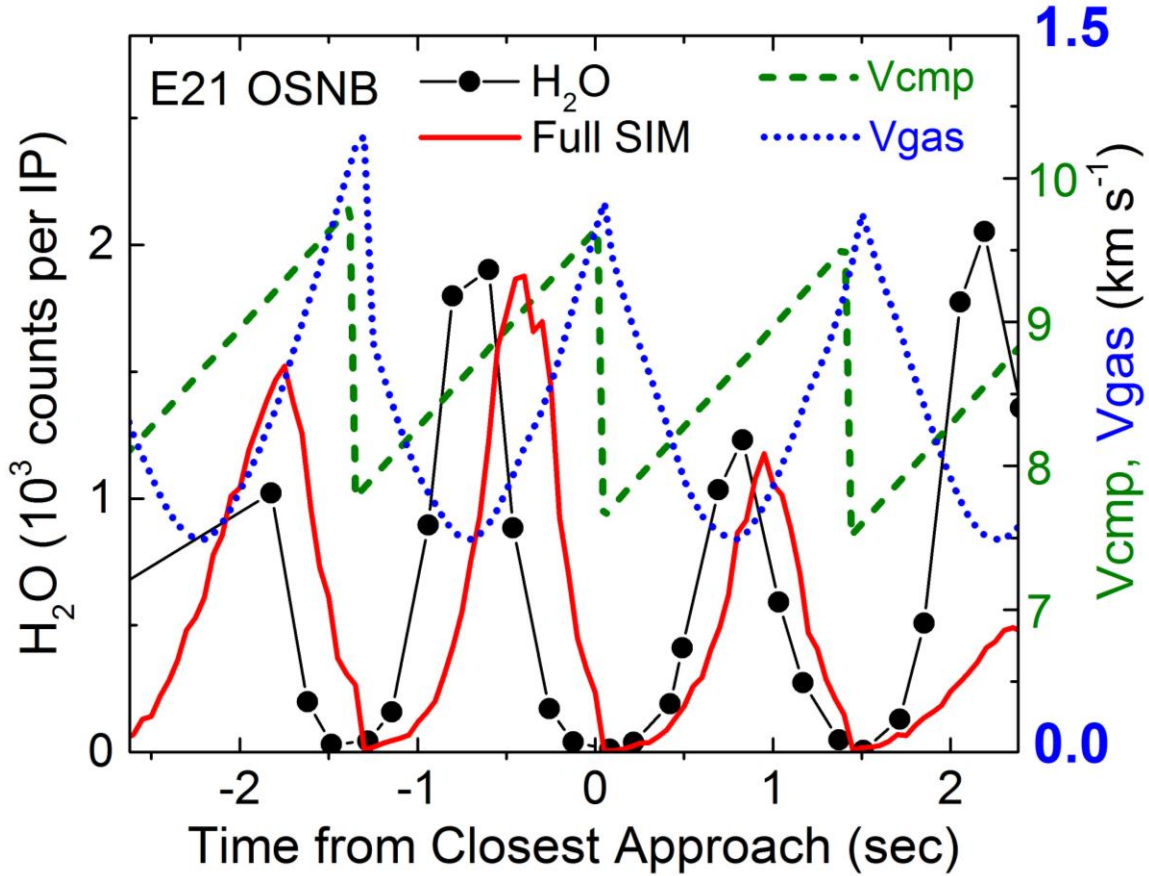


Fig. S10. Modeling of the plume H_2O OSNB signal. Observed (black circles) and simulated (red solid line) H_2O counts per INMS IP (31 ms) versus time from closest approach. A simulated OSNB H_2O profile for E21 was produced by modeling the Enceladus plume with 85 K H_2O vapor using INMS CSN density data from the E18 flyby, with tiger stripe jet sources from (41). The green dashed line shows the value of the instrument velocity filter (V_{cmp}) setting. The spacecraft speed is 8.5 km s^{-1} . The blue dotted line shows the magnitude of the velocity filter vector after translation to the Enceladus frame of reference (V_{gas} ; with 0-1.5 km s^{-1} plot scale labeled in blue text).

The H_2O signal is best modeled by water vapor at $85 \pm 30 \text{ K}$ (Fig. S11), which requires a ~ 0 to $\sim 2 \text{ km s}^{-1}$ range in water vapor bulk velocity when assuming a jet Mach number range of 0 to 8, as predicted by the plume outflow model. As can be seen in Fig. S10, the modeled peak amplitudes and positions do not agree exactly with the data, reflecting a combination of modeling uncertainty and possible temporal changes in the plume between previous Enceladus flybys and E21. Other secondary factors influencing

the change of H₂O signal during a scan include the changing relative sensitivity to different tiger stripe locations during a scan as the sensitivity function's surface projection sweeps across the tiger stripes, and the changing fraction of the sensitivity function that does not map to any tiger stripe (a phenomenon which we designate the 'geometrical effect'). As shown in Figs. S10 and S11, the maxima also exhibit variability between consecutive velocity scans as a result of spatial structure (indicative of discrete vapor sources or jets) of the plume vapor density along Cassini's trajectory.

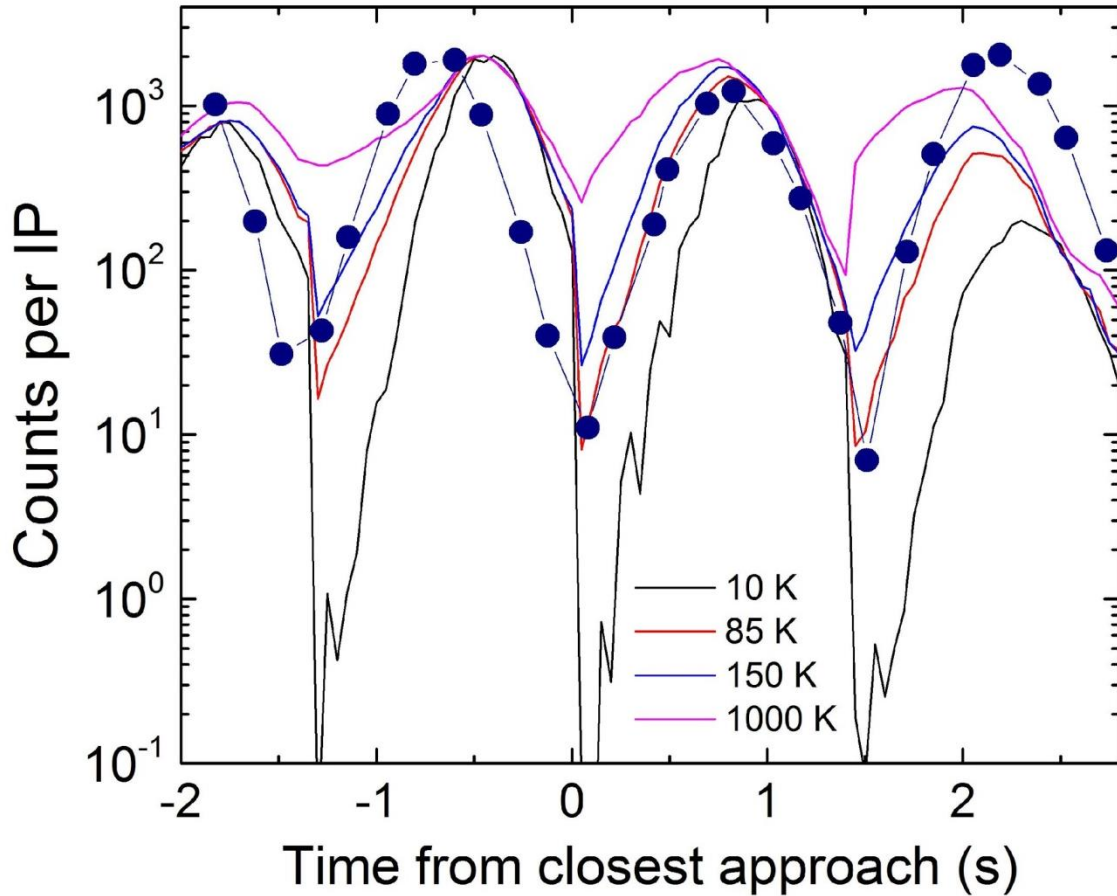


Fig. S11. Effects of H₂O vapor temperature on OSNB data near closest approach. Same as Fig. S10 near closest approach (dots: H₂O OSNB data), but on a logarithmic scale and with different model values (lines) for the H₂O vapor temperature. The data are consistent with H₂O vapor at 85 ± 30 K, corresponding to a bulk velocity distribution in the range ~ 0 to 2 km s^{-1} .

2.4. Estimating the magnitude and uncertainty in the H₂ to H₂O ratio

The H₂ signal response is less sensitive than H₂O's to the velocity scans for two reasons: i) the velocity acceptance for H₂ is much wider than that for H₂O ($\sim 5.3\text{-}9.7 \text{ km s}^{-1}$ vs. $7.0\text{-}9.0 \text{ km s}^{-1}$, respectively; section 2.2); and ii) the H₂ velocity distribution is broader than that of H₂O and therefore has a shallower slope. As a result, for a

collisionless model the H₂ signal is predicted to exhibit a sawtooth pattern corresponding to the velocity filter scans (Fig. S12). This response is dictated by the geometrical effect; that is, it is dominated by the fraction of the sensitivity that maps to the tiger stripes (which as it happens, increases during each scan).

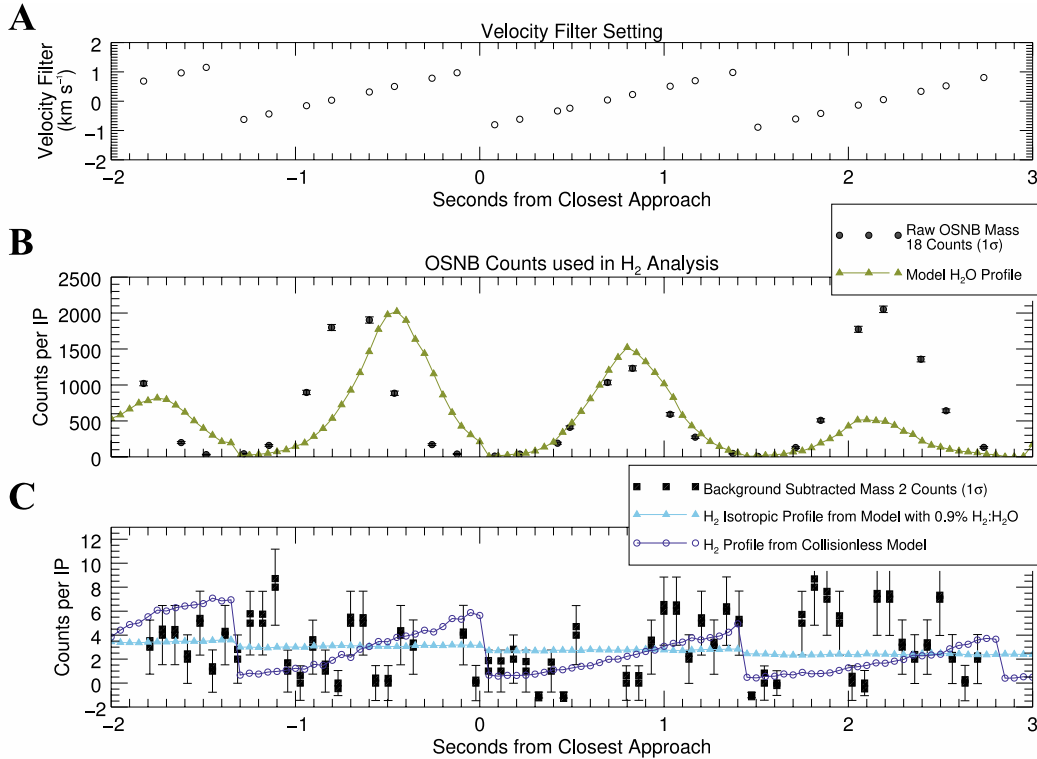


Fig. S12. Comparison of E21 modeled profiles and observed signal. A: The velocity filter setting varied between -1 and +1 km s⁻¹ relative to the spacecraft speed of 8.5 km s⁻¹ near closest approach. Modeled fits to the H₂O (B) and H₂ (C) gas distributions were used to derive the H₂ to H₂O ratio in the plume gas. The velocity filter setting (A) shows the sawtooth scans. For H₂, we compared the OSNB background-subtracted counts (black squares) near closest approach to two models: a collisionless model (purple circles), which assumes direct H₂ flux from the tiger stripes to the spacecraft, and a model of an isotropic H₂ distribution (blue triangles) that may result from intermolecular collisions in the plume.

A major difference between H₂O and H₂ is the effect of intermolecular collisions on the directionality of the molecular flux reaching Cassini INMS. Nearly all such collisions involve at least one H₂O molecule, since H₂O is the most abundant plume species (Table 1). Intermolecular collisions are in principle important because the mean free path (mfp) in the plume is only ~10 km, which is less than the 49 km closest approach altitude of the E21 flyby. Yet, in a binary H₂O-H₂O collision where both particles have equal mass, momentum conservation does not allow for H₂O to be scattered toward Cassini with a high scattering angle. Accordingly, even the scattered H₂O flux will arrive at Cassini from approximately the direction of the Enceladus tiger

stripes, and thus the H₂O velocity distribution seen by Cassini is well-approximated by the model of a collisionless plume. On the other hand, in an H₂-H₂O collision, the unequal masses allow for high H₂ scattering angles. Therefore, unlike H₂O, the H₂ flux should appear to be highly isotropic given Cassini's altitude of ≥ 49 km, which significantly exceeds the ~ 10 km mfp.

In Fig. S12, we predict the OSNB signal response to an isotropic H₂ velocity distribution. We have convolved the OS sensitivity function with an isotropic Maxwellian for an H₂ velocity distribution corresponding to 150 K and shifted in velocity space by the spacecraft speed. By making the distribution isotropic, we have removed any correlation of the H₂ velocity distribution with the tiger stripe source locations, aside from a scale factor associated with the H₂ density. The modeled H₂ signal is smooth, evolves in accordance with the plume gas density along Cassini's trajectory, and exhibits little response to the velocity filter scans. The data are consistent within statistical error with both the collisionless and isotropic models, but the short (~ 10 km) H₂ mfp makes the isotropic model more plausible. The model does not reproduce the "random" variability in the H₂ signal, which is attributable below 10 counts per IP to statistical noise. Using a scaling factor, we adjust the model to correspond to the average of the background-subtracted H₂ signal observed within ± 3 sec of closest approach. This model yields an estimated H₂ mixing ratio in the plume of 0.9% with an uncertainty of $\pm 0.5\%$ (Fig. S12). This is a conservative estimate, since we have not included the large H₂ spikes above 10 counts per IP in the model. The spikes may be attributable to spatial variability in H₂ backscattering and/or H₂ gas density along Cassini's trajectory, which are not considered in the isotropic model.

3. Gaseous plume composition from INMS

3.1. E14, E17, and E18 as context for E21

Enceladus flybys E14 (2011-274), E17 (2012-087), and E18 (2012-105) provided the INMS instrument with its most robust CSN data sets. The trajectories of all three flybys followed a nearly identical path through the plume source region perpendicular to Enceladus' south pole at nearly the same spacecraft velocity (~ 7.5 km s⁻¹) relative to the moon within a relatively short time span (a few months). These conditions allowed INMS to gauge its precision in measuring the plume composition, which we assume to be effectively constant given the measurement conditions and a persistent plume. The consistency of these conditions was in contrast to the very different measurement conditions of the previous flybys E3 (2008-072) and E5 (2008-283), which had trajectories following the outgoing plume gas at significantly higher spacecraft velocities (~ 14.4 km s⁻¹ and ~ 17.7 km s⁻¹, respectively).

We found that the accumulated plume mass spectra show a significant velocity-dependence in the measured composition. At high spacecraft velocity, this manifests in a larger proportion of plume material that we attribute to complex organic species (C₂H_x, C₃H_x, etc., as well as possible O- and N-bearing compounds). We hypothesize that this velocity-dependent change in composition is the result of energetic impacts of incoming ice grains and heavy organic molecules on the CSN antechamber. The impacts result in fragmentation of the incoming material and the release of raw titanium that alters the

gaseous composition that is transmitted to the INMS detector. These effects appear clearest in the case of increased H₂ production via H₂O reaction with Ti⁰, which is released in greater quantities at higher velocities (19). Impact chemistry appears to be responsible for the differences in the observed plume composition between the fast (E3 and E5) and slow (E7, E14, E17, E18, and E21) flybys. Since the E14, E17, and E18 flybys share the lowest plume encounter velocity, these data represent the least-altered plume composition and can be considered as the most representative CSN measurements of the true composition.

Owing to the velocity effect and trajectories that provided longer periods of exposure to plume material, the signal-to-noise ratio for most mass channels was found to be lower during the E14, E17, and E18 flybys when compared to the faster E3 and E5 flybys. For the low velocity flybys, mass channels above $m/z = 50$ u are populated only by counts due to noise. In contrast, E5 showed clear evidence of organic species as complex as C₆H₆ [masses 60-80 (19)]. However, we found that the accumulated plume mass spectra for E14, E17, and E18 are remarkably consistent when normalized to mass 18. Taking into account both the measurement uncertainties for each flyby and the variability between the three low-velocity flybys yields a total uncertainty of ~30% for the majority of the mass channels. Due to the consistency of the plume encounter conditions and observational data, we combine the accumulated plume mass spectra from E14, E17, and E18, and analyze the summed spectrum as representative of the plume composition.

3.2. Major identified plume species from the closed source

To provide a point of comparison for CSN measurements from E21, which are less frequent and therefore more uncertain, we describe the determination of the major volatile content of the plume for the combined mass spectrum of E14, E17, and E18. Mixing ratios are determined from measurements obtained throughout the flyby and during desorption of plume material. We use the term “anchor mass” to denote a mass for which a single given species provides a critical amount of the total observed signal; the number of counts at the anchor mass(es) predominantly determines the derived density of that species. The anchor mass is always related to a major fragment ion created by electron-impact dissociation of the species, though the parent ion may not be represented in the list of anchor masses. For example, the abundance of CH₄ is determined primarily from its mass 15 and 13 fragment ions, and not its parent ion at mass 16.

Major species are defined as those for which very little ambiguity in composition exists for the accumulated mass spectra of the plume. In other words, there are no other species that can replace the contributions of major species while still fitting the observed spectrum. Below is a summary of our derivation of the abundances of these species from the observed spectrum via anchor masses, in the order in which they are modeled.

H₂O dominates the signal at masses 18 and 17 (100% and 95% of the signal, respectively), and contributes around 45% of the signal at mass 16. H₂O also contributes to masses 19 and 20 through its heavy isotopologues.

CO₂ dominates the signal at mass 44, and its doubly-charged parent ion is observed at the typical level at mass 22. CO₂ also contributes ~7% of the signal at mass 28 by dissociation to CO.

CH₄ is determined primarily from masses 15 and 13, for which it contributes 90% of the total signal at both masses. However, CH₄ cannot account for the entire signal at its parent ion mass of 16.

NH₃ is determined from residual mass 16, where it contributes ~35% of the total signal. H₂O, CH₄, and CO₂ together do not adequately account for the total mass 16 signal. Since CH₄ is not produced as a major fragment of heavier hydrocarbons, other candidate hydrocarbons do not significantly impact the signal at mass 16. Likewise, other oxygen-bearing species can contribute only minimally via dissociatively-produced O⁺ ions. The significant residual at mass 16 implies a lack of ambiguity in the detection of NH₃, though the reliance on a lower proportion of the total signal at its anchor mass is reflected in a larger uncertainty in the abundance.

H₂ accounts for ~80% of the total signal at mass 2. The other primary contributor at mass 2 is dissociation of H₂O, which is responsible for ~18% of the total signal. All other H-bearing candidate species can provide only minor contributions to the mass 2 signal. Most of the CSN mass 2 signal must be from H₂ that is native to the plume, or produced by the reaction of H₂O with the titanium antechamber (19). Since the derived mixing ratio of H₂ from the open source (~0.9%; Table 1) is much lower than that from the closed source (~15%; Table S2), we deduce that the dominant source of H₂ for the CS is H₂O-Ti⁰ impact chemistry. This means that the native H₂O abundance can be recovered as the sum of the CSN abundances of H₂O and H₂ (19).

The results of forward modeling (19) to fit the summed mass spectrum are provided in Table S2. We find consistency in terms of the major plume composition measured by CSN between the E14, E17, E18, and E21 flybys. This suggests that there is nothing unusual about the E21 data, which provides confidence that we can combine them with the more plentiful measurements from E14, E17, and E18 to obtain a more complete understanding of the plume composition. Table 1 was made by combining CSN results from Table S2 with the H₂ mixing ratio from OSNB (section 2.4).

Table S2. Major volatile content of the Enceladus plume from the closed source. The derived compositions are based on CSN observations from E14, E17, E18, and E21. The number of counts at the anchor masses and other significant masses were used to determine the species abundances. The ranges in the E14, E17, and E18 values account for both measurement accuracy and variability between the three flybys. For E21, the low sampling frequency for CSN measurements during the flyby precludes accurate uncertainty estimation.

Chemical species	H ₂ O	CO ₂	CH ₄	NH ₃	H ₂
Anchor masses	18, 17	44	15, 13	16	2
Other significant masses	19, 20	22, 28	16	17	-
Volume mixing ratios (E14, E17, E18)	>84%	0.3%-0.8%	0.1%-0.3%	0.4%-1.3%	12%-18%
Volume mixing ratios (E21)	>90%	0.3%	0.3%	0.7%	9%

3.3. CSN observations used in testing the origin of H₂

We report upper-limit constraints on the plume abundances of ⁴He, ³⁶Ar, and O₂ from the combined E14, E17, and E18 CSN mass spectrum. ⁴He and ³⁶Ar produce their primary signals at masses 4 and 36, respectively. Neither of these mass channels displayed any clear signal above noise levels during the plume crossings. Both doubly-charged ions ⁴He⁺⁺ ($m/z = 2$ u) and ³⁶Ar⁺⁺ ($m/z = 18$ u) would be masked by the dominant signals of H₂ and H₂O, respectively. Thus, only upper limits can be derived for ⁴He and ³⁶Ar based upon the sum of the background noise during the nominal signal summation period (± 1000 sec of closest approach). The upper limits for ⁴He/H₂O and ³⁶Ar/H₂O are found to be $<0.006\%$ and $<0.0004\%$ by volume, respectively, in the plume gas. No other candidate species produce signal at mass 4, and only minimal signal can be expected at mass 36 from minor species that may be present above noise levels (C₃H₄ can produce the most signal, but $<30\%$ of the summed background noise).

Determining an upper limit for O₂ requires a more in-depth analysis. We found that mass 32 exhibits a very small increase in counts within ± 100 sec of the plume crossing. This increase could be attributed to incoming plume gas but is not a clear detection. Mass 32 also shows a distinct increase in signal that peaks hundreds of seconds after the plume encounter, and decays at a very slow rate before returning to background levels after two hours. This post-plume signal increase and resilient signal tail is interpreted as an artifact that is thought to be related to surface processes in the CS antechamber, as previously discussed for H₂O and H₂ (19).

The proposed artifact interferes with the nominal signal summation period. To isolate any native mass 32 signal, we use an abbreviated summation period of within ± 100 sec of closest approach for mass 32 only. This period appears to be outside the influence of the artifact, and includes the period over which the vast majority of observed plume gas enters the instrument. To correct for an underestimation of signal due to the shorter summation period, we multiplied the summed mass 32 signal by a factor of 2.5. This factor was determined by comparing summed signals for unpolluted masses of similar signal quality (i.e., those that show plume-related signal at low counting rates but also include substantial noise; e.g., mass 40), and it provides a conservative upper limit on the magnitude of increase in summed signal from the abbreviated (± 100 sec) to the nominal (± 1000 sec) summation periods. For the corrected mass 32 summed signal, we find that CO₂ would provide $\sim 30\%$ of the signal, and CH₃OH (methanol) could provide up to 25%. This leaves O₂ to provide about 45% of the mass 32 signal, corresponding to an O₂/H₂O number ratio of $\sim 0.004\%$. However, we consider this to be an upper limit for native O₂ in the plume rather than a firm detection, owing to the poor evidence for plume-related signal above noise. Also, we cannot rule out the possibility of catalytic conversion of a very small amount of plume H₂O to O₂ on the walls of the instrument's antechamber.

We also searched for non-plume H₂ and O₂. The E13 flyby (2010-355) provided low-altitude observations over Enceladus' northern hemisphere away from the south polar plume. This flyby had a closest approach altitude of ~ 48 km at $\sim 60^\circ$ N with a relative velocity of ~ 6.2 km s⁻¹. It is the only close flyby away from the plume with proper pointing for the INMS instrument. During this flyby, the CSN measurements appeared to only detect a distribution of ice grains. Masses 18 and 17 (H₂O) showed a

visible increase above background levels as Cassini approached Enceladus' northern surface, along with sharp signal spikes indicative of grains. Some other mass channels also showed signal spikes associated with the inferred grains, but no masses other than 18 and 17 displayed a detectable signal increase above background levels as a function of altitude. Because neither mass 2 nor mass 32 showed evidence of an altitude-dependent change in signal during the E13 flyby, we conclude that there is no detectable surface-derived H₂ or O₂ in the north.

3.4. Upper limits on N₂ and CO from OSNB observations

We discuss using the OSNB signal at mass 28 as a means of setting upper limits on N₂ and CO in the Enceladus plume. There were no OSNB counts above the background for molecules with $m/z = 28$ u. However, there were OSNB counts for mass 44 (Fig. 1), consistent with the CO₂ mixing ratio derived from CSN mode (Table S2). This consistency shows that species native to the plume gas produce signal in both modes. Therefore, the lack of counts at mass 28 in the open source implies that a large part of the signal seen in CSN mode at mass 28 (14, 19) must arise from a chemical source in the CS, such as fragmentation of large organic molecules or materials embedded in ice grains.

Based on the CSN peak count rates of 4000 at 28 u and a CSN/OSNB ratio of 400 to 500, the expected peak OSNB count rate near closest approach for 28 u would be 8 to 10 counts per IP at each IP in which the velocity compensation settings were optimized for the detection of slow, near-vertical-velocity molecules. These are the same velocity compensation settings that correspond to the maximum count rates for OSNB measurements of H₂O and CO₂. Using the peak OSNB H₂O count rate of 2000 and a conservative value of 1 count per IP as an upper limit for OSNB 28 u measurements, the upper bound for vapor molecules with a mass of 28 u is $1/2000 = 0.05\%$ of the H₂O number density. In other words, because no OSNB mass 28 was detected above background (the background rate corresponds to a fraction of 1×10^{-4}), there is only a 5% probability that the number density of mass 28 species is as high as 5×10^{-4} with respect to H₂O. This limit is less than 10% of the mixing ratio derived from CSN measurements (~ 0.009), and indicates that more than 90% of the CSN counts at 28 u do not come from native 28 u species. The combined mixing ratio of N₂+CO+C₂H₄ is $< 5 \times 10^{-4}$ from INMS, which is consistent with (24, 43).

Supplementary Text

4. Assessment of natural sources of H₂ in the plume

We have identified two general types of sources of H₂ on Enceladus. The first is primordial H₂ from the solar nebula, which can be hypothesized to have accreted directly as a gas or trapped in water ice. The second is production of H₂ on Enceladus. We discuss formation of H₂ via pyrolysis of organic materials and cracking of NH₃. We also consider conversion of H₂O to H₂ (plus a form of O) via radiolytic reactions on the surface or in the rocky core, via tectonic processes in the ice shell, or via coupling to the oxidation of reduced minerals in geochemical (e.g., hydrothermal) environments. Finally, we discuss

storage vs. active production of H₂ in the rocky core of Enceladus. In this section, we present arguments and models that can be combined with the INMS data to constrain the source of H₂ in Enceladus' plume.

4.1. Mechanisms of obtaining primordial H₂

4.1.1. Gravitational capture of nebular gas

If it formed before the dispersal of the solar nebula, Enceladus might have captured gas that was mostly molecular hydrogen (44); it does not matter to this argument whether the gas was captured from a subdisk around Saturn or the solar nebula itself. However, this hypothesis is inconsistent with the low mass of Enceladus. Put simply, Enceladus is too small to have captured gas from the solar nebula (45). Even Titan, which is $\sim 10^3$ times more massive than Enceladus, could not capture and retain primordial H₂. While Titan's atmosphere contains H₂, it is not primordial but instead a product of CH₄ photochemistry as evidenced by its supersolar D/H ratio (46), and the presence of hydrocarbons with a lower H/C ratio than CH₄ (e.g., C₂H₆, C₂H₂) that requires photochemical production of H₂ to achieve a mass balance of hydrogen. Also, the lack of detection of helium in the plume at Enceladus is inconsistent with a primordial origin of H₂. Gravitational capture of nebular gas would result in a Solar System ratio of $^4\text{He}/\text{H}_2 \approx 0.2$ (44). For an H₂ mixing ratio of 0.4-1.4% in the plume gas (Table 1), the ^4He mixing ratio would be 0.08-0.28%, which exceeds by over one order of magnitude the upper limit (<0.006%) from INMS (section 3.3). The implication is that at most 7.5% of H₂ in the plume could be accreted as gas. We conclude from these two independent lines of evidence that the observed H₂ was not gravitationally captured from the solar nebula.

4.1.2. Trapping in cold amorphous ices

Enceladus could have obtained primordial H₂ if its icy building blocks formed at very low temperatures, as amorphous water ice can trap H₂ below 20 K (29). However, there are several concerns regarding this mechanism as a source of present-day H₂. First, there is a lack of empirical analogues among comets. Current cometary observations do not indicate that such cold planetesimals existed in the outer Solar System. Nuclear spin temperatures derived from ortho/para ratios of cometary H₂O and NH₃ all exceed ~ 20 K (47). Moreover, known comets are depleted relative to the solar composition in various species (e.g., ^{36}Ar , N₂) that are less volatile than H₂ (28, 48). The cometary observations also suggest clathrate hydrates rather than amorphous ices as the carriers of these volatiles (49), and clathrates are less effective carriers of H₂ (22).

There is also a problem of retaining primordial H₂ to the present day because ice is not a robust storage medium for H₂. Amorphous ice releases H₂ when heated: 67% is lost between 16 and 35 K, 11% between 35 and 85 K, and 22% between 85 and 150 K (29). For comparison, subsolar surface temperatures on Enceladus are ~ 80 K (50), and the bottom of the ice shell is bounded by a liquid water ocean at ~ 270 K (11, 25). Any accreted H₂ should be expelled from the ice by degassing as the amorphous ice converts to crystalline ice. Even in the upper layers of the ice shell where some amorphous ice might linger (51), exposure to vacuum in pores may cause outgassing of any remaining

H₂. To persist in the crust, H₂ would need to be stored as a clathrate hydrate, and the formation of H₂ clathrate requires high pressures of H₂ [>1000 bar; (22, 23)]. However, pressures in the ice shell cannot be so high because of the small size of Enceladus. The lithostatic pressure ~ 20 km below the surface, corresponding to the base of the ice shell in the model of (11), is only ~ 20 bar.

Alternatively, one can imagine trapping of H₂ at lower pressures in multi-guest clathrates stabilized primarily by CH₄ and/or CO₂, two of the major non-water species in the plume (Table 1). However, clathrates have a strong preference for CH₄ and CO₂ over H₂. To assess the potential contribution of H₂ from multi-guest clathrates, we consider the experimental results of (52), which show that H₂ only occupies between 0.3 and 2.3% of small cages depending on the temperature, total pressure, and composition of the system. In the case of Structure I clathrate (the most stable form for CH₄ and CO₂), there are 2 small cages for every 6 large cages (53). Assuming a large cage occupancy of 95% and a small cage occupancy of 0-30% for CH₄+CO₂ (53), the gas mixture released by dissociation of this clathrate would have an H₂/(CH₄+CO₂) ratio of $(1-8)\times 10^{-3}$. In the more favorable case of Structure II clathrate (16 small cages and 8 large), this ratio would be $(0.4-5)\times 10^{-2}$. The Enceladus plume was observed to have an H₂/(CH₄+CO₂) ratio ranging from 0.4 to 3.5 (Table 1), significantly higher than the range of values predicted for multi-guest clathrates. Even Structure II clathrate could contribute at most $\sim 13\%$ of the observed H₂. Whether such a clathrate reservoir exists in the icy crust (54), it is not the main source of H₂ measured by INMS in the plume.

If primordial H₂ were somehow accreted and retained by Enceladus anyway, the plume would contain significant amounts of other primordial volatiles. We develop a simple model that quantifies this scenario. At temperatures low enough to trap H₂ in amorphous ice [<20 K (29)], primordial Ar, CO, and N₂ would be fully accreted (55). We can estimate their abundances relative to trapped H₂ by adopting an endmember model of a kinetically inhibited solar nebula, where the bulk composition is assumed to be solar (Table S3), and all of the carbon and nitrogen are in CO and N₂, respectively (56). Magnesium and silicon are included because they are the most abundant sinks of oxygen among the rock-forming elements. The speciation of oxygen determines the abundance of H₂O via: $O_{\text{total}} = \text{H}_2\text{O} + \text{CO} + \text{MgO} + 2\text{SiO}_2$. The abundance of trapped H₂ can be estimated by assuming that the H₂/H₂O ratio could be as high as 0.63 (29). Using this value, we calculate mixing ratios of ³⁶Ar, CO, and N₂ that would be observed in the plume if the H₂ were acquired by trapping in amorphous ices (Table S4).

Table S3. Solar system abundances of volatile elements and oxide-forming metals. Data are taken from (44) and reported with respect to 10^6 atoms of Si.

Element	Symbol	Molar abundance
Argon-36	³⁶ Ar	8.671×10^4
Carbon	C	7.079×10^6
Magnesium	Mg	1.020×10^6
Nitrogen	N	1.950×10^6
Oxygen	O	1.413×10^7
Silicon	Si	1.000×10^6

Table S4. Volatile content of <20 K amorphous ice vs. INMS observations of Enceladus’ plume. Expected abundances of key volatile species in the Enceladus plume if H₂-bearing amorphous ices had been accreted are compared to upper limits from INMS (sections 2.4, 3.3, and 3.4).

Species	Relative molar abundance in cold amorphous ices *	Mixing ratio in plume for cold amorphous ice model	Observed mixing ratio in plume
³⁶ Ar	>0.034	>0.01%	<0.0004% ‡
CO	>2.79	>1%	<0.05% §
N ₂	>0.38	>0.15%	<0.05% §
H ₂	1	0.4-1.4% †	0.4-1.4% §

*Based on experimental trapping of H₂, and complete condensation of the other species from a solar composition gas; †Set to the observed range to enable scaling for the other species; ‡, From the closed source; §From the open source.

The predicted mixing ratios for ³⁶Ar and CO are significantly higher than the upper limits derived from INMS data. The predicted mixing ratio for N₂ may be somewhat higher than its upper limit, depending on the value of the H₂ mixing ratio (Table S4). However, the accretion model abundances would be increased if H₂ trapping were less efficient than the assumed maximum, which would lead to larger discrepancies between this model and the detection limits. The upper limit on the abundance of ³⁶Ar in the plume (<0.0004%; section 3.3) implies that an accreted ice source could provide to the plume an H₂ mixing ratio of <0.01%, based on ³⁶Ar/H₂ >0.034 for such a source (Table S4). We conclude that the source of H₂ in the plume is not primordial H₂ that was trapped in amorphous ice.

4.2. Mechanisms of producing H₂ on Enceladus

4.2.1. Generation of H₂ via pyrolysis of organics

We attempt to constrain the amount of H₂ that could be formed from heating accreted organic matter in Enceladus’ rocky core. We consider insoluble organic matter (IOM) in carbonaceous chondrites as a potential analogue of primordial organic matter on Enceladus. We find that the most relevant available data are from (57), who performed dry pyrolysis experiments of IOM from the Murchison CM2 meteorite. We are not aware of any reports of H₂ yields from hydrous pyrolysis experiments, which could be more relevant to Enceladus. Okumura and Mimura (57) measured the yield of H₂ as a stepwise function of temperature. The integrated yield of H₂ up to the temperature (T in K) of interest from their experiments can be represented by the equation

$$\log\left(\frac{\text{mol H}_2}{\text{kg IOM}}\right) = 3.95 - \frac{4023}{T}, \quad (\text{S10})$$

from 623-1073 K (350-800°C) with an accuracy to within a factor of ~2. Their starting IOM had an organic bound hydrogen content of 30 moles per kg of IOM (57), so the fraction (f) of the initial organic H that is converted to H₂ can be expressed as

$$\log f = 2.78 - \frac{4023}{T}, \quad (\text{S11})$$

which ranges from 0.02-10% between 623 and 1073 K. Similarly, (58) reported H₂ yields of ~4 mg per gram of organic carbon from vacuum pyrolysis experiments of Murchison and Orgueil (CI1) at 600°C. For IOM containing 67 wt. % C and 3.5 wt. % H [the average of Murchison and Orgueil; (59)], the corresponding yield of H₂ is ~8%. This falls within the previous range.

It is not straightforward to apply these results to Enceladus because the experiments were performed at high temperatures over timescales of minutes at most. In contrast, on Enceladus such pyrolytic processes may occur at lower temperatures but potentially over much longer timescales, such as millions to billions of years. Because of these uncertainties, it is most conservative to adopt the full lab-based production efficiency of 0.02-10% for H₂ as a possible range.

To calculate the total amount of H₂ that could be generated from pyrolysis of primordial organic matter, an estimate is needed for the accreted mass of IOM on Enceladus. The mass of rock in Enceladus' core has been estimated to be 6.3×10^{19} kg (Table S9, section 4.2.5). If the rock is assumed to contain a percentage of organic carbon in IOM similar to that in CI chondrites (the most organic-rich meteorites), there would be ~2 wt. % C_{organic} in the rock (59), equivalent to ~4 wt. % IOM. Therefore, for a CI chondrite-like content of IOM, the accreted inventory of IOM on Enceladus would be $\sim 2.5 \times 10^{18}$ kg containing $\sim 7 \times 10^{16}$ kg ($\sim 7 \times 10^{19}$ moles) of organic hydrogen. We also consider an abundance of $\sim 70 \times 10^{19}$ moles of H_{organic} to account for the possibility that Enceladus may be more like comets in terms of the accreted organic inventory (60). Using the above ranges for the amount of organic H and the production efficiency of H₂ from organic H, it is found that $(0.07-350) \times 10^{17}$ moles of H₂ could be produced from accreted organic matter on Enceladus. This has the potential to sustain the present outgassing rate of H₂ in the plume ($[1-5] \times 10^9$ mol H₂ yr⁻¹) for up to ~30 Gyr (i.e., much longer than the age of the Solar System). Thus, organic pyrolysis can be a robust source of H₂.

4.2.2. Cracking of NH₃

To assess the possible role of cracking of NH₃ in the production of H₂ inside Enceladus, we consider the following net reaction



which yields 3 moles of H₂ for every mole of N₂. From open source observations, the upper limit for the mixing ratio of N₂ in the plume gas is <0.05% (section 3.4). If all of this N₂ were derived from NH₃, the maximum contribution of H₂ to the plume from Rxn. S12 would be 0.15%. However, the observed mixing ratio of H₂ in the plume is 0.4 to

1.4% (Table 1). This suggests that less than half of the H₂ [and probably much less if Rxn. S12 is kinetically inhibited; (16)] can be derived from the thermal decomposition of NH₃. The presence of a significant amount of NH₃ gas in the plume (Table 1) also seems to argue against the occurrence of appreciable depletion of NH₃ by Rxn. S12. Hence, cracking of NH₃ is not supported as an important source of H₂ for the plume.

4.2.3. Radiation-induced decomposition (radiolysis) of water

We investigate whether production of H₂ by radiolytic reactions on the surface or in the core of Enceladus could explain the observations of H₂ in the plume.

4.2.3.1. Water ice on the surface

Radiolysis of water ice on the surface of Enceladus can produce H₂ in two different ways. The first is dissociation of H₂O to O₂ and twice as much H₂. The second is hydrogen peroxide formation caused by penetration of energetic electrons



with the possibility of H₂O₂ being transported down into Enceladus' ocean and dissociating there into additional O₂ + H₂ (0.5 O₂ + H₂O more likely).

To estimate the rates of production from these processes in moles per year, we used the model detailed in the supporting online material for (61), considering an ambient plasma density of 70 water group ions cm⁻³ at an equivalent temperature of 35 eV. The radiolytic yields are derived from laboratory experiments (61 and references therein). The presence of refractory impurities can inhibit surface O₂ and H₂ production (62), but to obtain an upper limit on the rates of O₂ and H₂ formation we considered the case of nearly pure H₂O ice on Enceladus' surface (51).

We calculate a global rate of production of H₂ of $\sim 6 \times 10^7$ mol yr⁻¹ due to H₂O dissociation in Enceladus' surface ice. Another $\sim 2 \times 10^7$ mol yr⁻¹ should be produced in the process of peroxide formation, and as a limiting case another $\sim 2 \times 10^7$ mol yr⁻¹ could be produced if all of the peroxide were cycled down into Enceladus' ocean and subsequently dissociated. The total of $\sim 1 \times 10^8$ mol yr⁻¹ is at least one order of magnitude below the $(1-5) \times 10^9$ mol yr⁻¹ required to account for 0.4-1.4% H₂ in the plume gas (Table 1). The amount of H₂ produced in just the south polar region (southward of 50° S) should be approximately one order of magnitude less than the global rate (based on surface area), which makes this mechanism even more discrepant.

An additional inconsistency with radiolysis of surface ice as a primary source of the observed H₂ is that this process would not be expected to produce an enhancement in the density of H₂ at the plume. Instead, a more globally homogeneous distribution of H₂ would be expected, as the whole surface is exposed to radiation. However, INMS detected H₂ only in the plume, and not elsewhere over Enceladus (section 3.3). Lastly, if the observed H₂ were derived from radiolysis of water ice, then the plume should have an O₂/H₂ ratio of $\sim 0.4-0.5$, equivalent to an O₂ mixing ratio of 0.15-0.7% (for an H₂ mixing ratio of 0.4-1.4%; Table 1), which is much higher than the observational upper limit of 0.004% for O₂ (section 3.3). There are no instrumental effects that would prevent the

detection of O₂ if present, as evidenced by the previous detections of O₂ at Rhea and Dione (62). Hence, surface ice radiolysis is an insignificant contributor to the detected H₂ in the plume.

4.2.3.2. Liquid pore water in the rocky core

We also need to consider radiolysis of liquid water in the subsurface by the decay of long-lived radioisotopes as a possible source of H₂. Because Enceladus' core is likely to be quite porous (Table S9, section 4.2.5), large amounts of water can be expected to be in contact with rocks. This would expose water molecules to alpha and beta particles, and gamma rays generated from the decay of long-lived radioisotopes that would be present if the core's composition is approximately chondritic. Below, we estimate the production rate of radiolytic H₂ in Enceladus' core.

This is done using the method of (32), which was developed for applications to Earth. In this method, the energy $D_{i,k}$ deposited in water (as opposed to that absorbed by rock particles) can be computed via

$$D_{i,k} = \frac{\rho_r A_k \sum E_{i,k}}{\frac{1}{1-\phi} + \frac{1}{S_i \phi}} \quad (\text{S14})$$

where i designates the type of particle emitted (alpha, beta, gamma), and k the radionuclide of interest; ρ_r is the grain density of the rock (g cm^{-3}), and A_k the activity of radionuclide k (decays $\text{s}^{-1} \text{g}^{-1}$ of rock), which is the product of the number of atoms of radionuclide per gram of rock times the decay constant; $\sum E_{i,k}$ represents the summed energy of particles i emitted by the whole decay series of radionuclide k [MeV; calculated by (32)], ϕ the porosity, and S_i the stopping power [for adopted values and details, see (63)].

The total yield of H₂ accounting for all types of decay i is given by

$$Y = \sum_{i,k} D_{i,k} G_i, \quad (\text{S15})$$

where G_i is defined as the H₂ yield per unit of energy for decay type i [molecules MeV^{-1} ; values taken from (64, 65)]. As for cases on Earth, we considered the decay of ⁴⁰K, ²³²Th, ²³⁵U, and ²³⁸U, using present-day CI chondritic abundances [respectively 94, 44, 0.086, and 12 $\mu\text{g kg}^{-1}$ of rock; (44)], where the values have been scaled to be consistent with the densities of the model hydrous rocks described in section 4.2.5. We also adopted bulk values for the porosity (27%) and grain density (3.0 g cm^{-3}) that are consistent with endmember models of a fully hydrated rocky core (Table S9, section 4.2.5). We assumed that the radioisotopes are predominately present in rocks rather than dissolved in Enceladus' ocean. This is supported by the low K content of salt-rich plume particles (25, 26). No analytical data are available for U and Th in the ocean, but Th minerals are generally insoluble in liquid water, and U minerals are insoluble under non-oxidized conditions (66). The detection of H₂ and the lack of detection of sulfate salts in the plume support the interpretation of non-oxidized conditions inside Enceladus (15). Using the

above model of radiolysis, we obtain a production rate of $(1-3)\times 10^8$ mol H_2 yr⁻¹ for the whole core of Enceladus, which is less than the value ($[1-5]\times 10^9$ mol H_2 yr⁻¹) implied by the observations of H_2 in the plume.

In addition, not all of the radiolytically produced H_2 would be outgassed if a significant volume of the core is impermeable. To explore this possibility, we calculated the characteristic length scale for diffusion as

$$L = (Dt)^{1/2}, \quad (S16)$$

where D denotes the diffusion coefficient and t time. Because the core is inferred to be rich in wet phyllosilicates (section 4.2.5), we adopted a diffusion coefficient for H_2 in water-saturated clay [$D \approx 5\times 10^{-10}$ m² s⁻¹; (67)]. For the most conservative case of $t = 4.56$ Gyr, we find $L \approx 10$ km, which is small compared to the dimensions of the core [~ 190 km radius; (10)]. This implies limited diffusive transport of H_2 , consistent with estimates of low permeability for aqueously altered carbonaceous chondrites (68) as possible geochemical analogues of Enceladus' core (69). If it is assumed that only the top 10 km of the core is in diffusive steady-state with radiolytic production of H_2 , then the release rate from the core can be approximated as $(1.5-4.5)\times 10^7$ mol H_2 yr⁻¹. Altogether, our estimates suggest that at most only a minor fraction (e.g., <10%) of the observed H_2 can be formed by contemporary radiolysis in the subsurface.

4.2.4. Cataclastic formation of H_2

Recent experiments suggest that H_2 can be produced by comminution (e.g., grinding) of silicate minerals in the presence of water in regions of shearing (30), such as active fault zones. Here, we investigate the possible contribution of this process to the production of H_2 at Enceladus. In extension fault zones (70) the large faults accommodate the bulk of the strain (71, 72), while most of the observable fractures reside in strain shadows and are inactive (73, 74). We therefore assume in the following calculation that the active tiger stripes contribute the majority of H_2 potentially produced by a comminution mechanism. This assumption of locally produced "tectonic H_2 " is in keeping with the localized nature of INMS observations of H_2 in the plume.

Hsu et al. (13) reported the detection of silica particles between 6 and 9 nm in radius. They proposed that those particles are embedded in ice grains ejected from Enceladus. For the present calculation, we assume that the reported range in size is representative for silica particles that may be loaded into ice in the south polar region by plume fallout. Based on a density of 2.1 g cm⁻³ for amorphous silica, we calculate a specific surface area for spherical particles between 160 and 240 m² g⁻¹. Telling et al. (30) used their experimental data to derive the following linear relationship between H_2 production (H_2 , in nmol g⁻¹) and molar silica surface area (SA , in m² g⁻¹)

$$H_2 = 15.34 \times (SA) - 0.19. \quad (S17)$$

It should be noted that silica particles from Enceladus have molar silica surface areas approximately two orders of magnitude larger than those from (30). Nevertheless, in the absence of more appropriate data we assume a linear extrapolation of Eq. S17, and

calculate an H₂ production between 2400 and 3700 nmol H₂ per g SiO₂. To account for possible non-linear behavior beyond the experimental data range in the relationship between H₂ production and molar silica surface area, we consider the expanded range 2400 to 37000 nmol H₂ per g SiO₂.

To convert this quantity to a rate, we assume that Si-O bonds are a reactant in the production of H₂ (30), and that deposition and consumption of Si-O bonds may be in a steady state (75). The model of (13) suggests that ice erupted and emplaced onto the south polar region may contain 150 to 3800 ppm SiO₂. For a water ice deposition rate in the tiger stripe region of order 1 to 10 kg s⁻¹ (76), the corresponding annual deposition is (3-30)×10¹⁰ g of ice per year. This suggests concurrent deposition of (4.5-1100)×10⁶ g of silica per year. Using a conservative range for H₂ production per mass of SiO₂ (see above), we estimate an H₂ production rate between 11 and 42000 mol yr⁻¹, which is negligible compared to the observed rate of (1-5)×10⁹ mol yr⁻¹ in the plume. We conclude that comminution is not a significant source of H₂ on Enceladus, because there is simply not enough silicon-bearing material (by several orders of magnitude) that is subjected to fault activity in the tiger stripes.

4.2.5. Aqueous oxidation of reduced minerals

Estimates for the magnitude of global H₂ production on Earth via aqueous alteration of rocks (e.g., serpentinization) are commonly based on models of representative reactions (31, 77). Similarly, we develop a mass balance model as a first-order constraint on the amount of H₂ that could be produced by water-rock reactions inside Enceladus. The problem can be broken down into two parts. First, we need to estimate the H₂ yield per kg of rock for representative geochemical reactions in Enceladus' rocky core (which are dependent on its mineralogy). Second, estimates need to be made for the total mass of rock inside Enceladus, which imposes a limit on the amount of H₂ that can be produced for the bulk body.

To simplify modeling of the mineralogy of Enceladus' core, we restrict ourselves to the Mg-Si-Fe-S-O-H system, which includes the most abundant rocky elements in chondritic material, and allows silicate hydration to be considered. We assume that the relative abundances of Mg, Si, Fe, and S are solar or CI chondritic (the adopted elemental composition is given in Table S5). We define four model rock mineralogies, each of which consists of some of the normative minerals given in Table S6. The selection of these minerals is guided by observations of chondritic meteorites (78), interplanetary dust particles (79), and cometary dust (80). The normative minerals are components of endmember-type models of possible rocks on Enceladus. The model rocks that are considered are termed accreted anhydrous rock (AAR), metamorphosed anhydrous rock (MAR), reduced hydrous rock (RHR), and oxidized hydrous rock (OHR). The minerals in each rock are listed in Table S7. Because each rock is assumed to contain only four representative minerals (the minimum number of minerals to obtain a normative mineralogy), it is simple to calculate the proportions of each mineral that satisfy mass balances for Mg, Si, Fe, and S.

Table S5. Solar system abundances of the most abundant rock-forming elements (excluding oxygen). Data are taken from (44) and reported with respect to 10^6 atoms of Si.

Element	Symbol	Molar abundance
Iron	Fe	8.380×10^5
Magnesium	Mg	1.020×10^6
Silicon	Si	1.000×10^6
Sulfur	S	4.449×10^5

Table S6. Minerals included in the mass balance model. The molar masses (μ) and densities (ρ) for minerals in normative models of past/present rocks on Enceladus are provided. A talc endmember is used to represent saponites for compositional modeling of simplified systems (16), but the talc/saponite component is assumed to have a saponite density based on the occurrence of saponite in potential chondritic analogues of Enceladus (69, 91). Mineral densities at 25°C and 1 bar are taken from (103).

Mineral	Abbreviation	Formula	μ (g mol ⁻¹)	ρ (g cm ⁻³)
Chrysotile	Ctl	Mg ₃ Si ₂ O ₅ (OH) ₄	277.09	2.56
Enstatite	En	MgSiO ₃	100.38	3.19
Fayalite	Fa	Fe ₂ SiO ₄	203.78	4.39
Forsterite	Fo	Mg ₂ SiO ₄	140.68	3.27
Greenalite	Gre	Fe ₃ Si ₂ O ₅ (OH) ₄	371.74	3.23
Iron metal	Fe-met	Fe ⁰	55.85	7.87
Magnetite	Mag	Fe ₃ O ₄	231.55	5.20
Pyrrhotite	Po	Fe _{0.875} S	80.94	4.62
Talc/Saponite	Tlc/Sap	Mg ₃ Si ₄ O ₁₀ (OH) ₂	379.24	2.30
Troilite	Tro	FeS	87.92	4.85

We consider four types of geochemical reactions that could lead to the production of H₂ inside Enceladus (Table S8). In these reactions, the model rocks are transformed into more oxidized rocks, with retention or mass balance of Mg, Si, Fe, and S in rocks. It is assumed that magnetite is the terminal form of oxidized iron, because further oxidation of magnetite to hematite/ferric oxyhydroxides is a negligible source of H₂ that would not be expected to lead to detectable H₂ in the plume, as a result of the low equilibrium H₂ fugacity (81). The amount of H₂O in each reaction is determined from an oxygen mass balance, and the theoretical yield of H₂ is calculated from a hydrogen mass balance. This sets the stoichiometry of the reaction, which can be used to compute the number of moles of H₂ per kg of reactant or product rock (Table S8).

Table S7. Mineral abundances in model rocks. Model rocks shown here represent possible compositions on Enceladus, and are assumed to contain solar abundances of the major rock-forming elements. Only one non-sulfide iron-bearing mineral is considered in each rock. Multiple ferromagnesian solid solutions may be present in reality.

Rock type:	Accreted anhydrous rock		Metamorphosed anhydrous rock		Reduced hydrous rock		Oxidized hydrous rock	
Abbreviation:	AAR		MAR		RHR		OHR	
Mineral	Wt. %	Vol. %	Wt. %	Vol. %	Wt. %	Vol. %	Wt. %	Vol. %
Chrysotile	-	-	-	-	48.86	57.17	27.53	32.30
Enstatite	60.63	72.47	31.48	36.79	-	-	-	-
Fayalite	-	-	26.98	22.92	-	-	-	-
Forsterite	1.73	2.02	20.29	23.14	-	-	-	-
Greenalite	-	-	-	-	29.75	27.59	-	-
Iron metal	13.53	6.56	-	-	-	-	-	-
Magnetite	-	-	-	-	-	-	19.11	11.04
Pyrrhotite	-	-	21.25	17.15	19.27	12.49	19.87	12.92
Talc/Saponite	-	-	-	-	2.12	2.76	33.49	43.74
Troilite	24.11	18.95	-	-	-	-	-	-
ρ (g cm ⁻³)	3.81		3.73		2.99		3.00	

Table S8. Oxidation reactions of Enceladus model rocks. Past/present H₂-producing geochemical reactions on Enceladus are given, based on transformations of representative mineral assemblages. The stoichiometric coefficients (in moles) are normalized to an initial mass of 1000 g of accreted anhydrous rock. Definitions of abbreviations for minerals and rocks are given in Tables S6 and S7, respectively. The rock masses in these models are: AAR = 1000 g, MAR = 1044 g, RHR = 1152 g, and OHR = 1117 g.

Abbreviated reaction	Reactants	Products
AAR + H ₂ O → RHR + H ₂	6.04 En + 0.12 Fo + 2.42 Fe-met + 2.74 Tro + 8.74 H ₂ O	0.06 Tlc/Sap + 2.03 Ctl + 0.92 Gre + 2.74 Po + 2.77 H ₂
AAR + H ₂ O → MAR + H ₂	6.04 En + 0.12 Fo + 2.42 Fe-met + 2.74 Tro + 2.77 H ₂ O	3.27 En + 1.51 Fo + 1.38 Fa + 2.74 Po + 2.77 H ₂
RHR → OHR + H ₂ O + H ₂	0.06 Tlc/Sap + 2.03 Ctl + 0.92 Gre + 2.74 Po	0.99 Tlc/Sap + 1.11 Ctl + 0.92 Mag + 2.74 Po + 1.84 H ₂ O + 0.92 H ₂
MAR + H ₂ O → OHR + H ₂	3.27 En + 1.51 Fo + 1.38 Fa + 2.74 Po + 4.13 H ₂ O	0.99 Tlc/Sap + 1.11 Ctl + 0.92 Mag + 2.74 Po + 0.92 H ₂

To estimate the amount of rock inside Enceladus, we adopt the internal structure model of McKinnon (10). The density of the rocky core from this model (2.45±0.1 g cm⁻³) is significantly lower than those of AAR and MAR, but not much lower than those of RHR and OHR (Table S7). Owing to its apparent low density, the core should not be composed of more than a minor fraction of anhydrous rock, consistent with laboratory experiments (82) and observations of carbonaceous chondrites (83), which demonstrate that silicate hydration (e.g., serpentinization) is geologically rapid. Geophysical modeling also suggests that Enceladus' entire core may be accessible to ocean-derived fluids, which would promote the hydration of silicate minerals (84). We can expect Enceladus' core to be extensively (but not necessarily completely) altered.

We consider an endmember model in which the core is composed of hydrous rock and pore water. The latter needs to be present because the core is apparently less dense than the hydrous rocks in Table S7. Otherwise, for the rocks to be less dense than computed, sulfide minerals would need to be oxidized to sulfate salts (e.g., MgSO_4), which have not been detected at Enceladus (25, 26). Calculated masses of water and rock in a porous, fully hydrated core are given in Table S9 for RHR and OHR, which have almost identical densities. This leads to a common mean porosity of ~25-30%, which could be expected for a small body (85). Some anhydrous rock could be added to the model if additional porosity is assumed, but a substantial anhydrous component can be excluded because the combination of abundant anhydrous rock and high fluid-filled porosity would be geochemically unstable with respect to silicate hydration over geologic time.

Table S9. Inferred physical properties of Enceladus' core. Mass and volume properties of Enceladus' core are calculated for two endmember compositions of hydrous rock (Table S7). The core is assumed to consist of hydrous rock and liquid pore water, and its properties are calculated to be consistent with the model of (10).

Core property	Reduced hydrous rock	Oxidized hydrous rock
Density of rock (kg m^{-3})	2990	3000
Density of water (kg m^{-3})	1000	1000
Core density (kg m^{-3})	2450	2450
Core porosity	27%	28%
Core radius (km)	190	190
Core volume (m^3)	2.87×10^{16}	2.87×10^{16}
Core mass (kg)	7.04×10^{19}	7.04×10^{19}
Mass of rock (kg)	6.26×10^{19}	6.25×10^{19}
Mass of pore water (kg)	7.80×10^{18}	7.90×10^{18}

Table S10 provides results that can be used to assess scenarios of present and integrated production of H_2 for three geochemical net reactions. The formation of MAR from AAR (Table S8) is not considered in Table S10, because this reaction may not be a significant source of H_2 in a core that is rich in hydrous rock [although it could be relevant to the early history of Enceladus if dehydrating conditions prevailed; (86)]. If AAR oxidation does not terminate at RHR but goes all the way to OHR, then the yields for $\text{AAR} \rightarrow \text{RHR}$ and $\text{RHR} \rightarrow \text{OHR}$ should be summed.

The upper limit for the amount of H_2 produced by aqueous alteration is $\sim 2 \times 10^{20}$ moles (Table S10). The results in Table S10 indicate that even slow reaction rates can account for the emission rate of H_2 in the plume. This can be illustrated by determining how long it would take to react a relatively small mass of rock (1% of the core's mass) at the required rates. This mass of reactant rock could support H_2 production at today's rate for geologically significant periods of hundreds of millions to potentially billions of years, depending on the particular reaction (Table S10). Aqueous oxidation of accreted anhydrous rock is a potent source of H_2 , but even rocks that were previously partially oxidized, such as reduced hydrous rock, have the potential to generate sufficient H_2 . This

is a consequence of the high abundance of iron in chondritic material (Table S5). A large amount of reactant rock is not needed to explain the observation of H₂ in the plume, and indeed a small to moderate amount (~2-40% of the core's mass, depending on the value of the H₂ mixing ratio) would be able to sustain the present level of H₂ release over the history of the Solar System (4560 Myr).

Table S10. Timescale and H₂ yield for model water-rock reactions. Rate-related data and theoretical yields of H₂ are provided for some water-rock oxidation-reduction reactions of relevance to Enceladus.

Abbreviated reaction *	Reaction rate of rock (kg yr ⁻¹) to match observed H ₂ †	1% Depletion time (Myr) ‡	Maximum yield of H ₂ (mol) §
AAR + H ₂ O → RHR + H ₂	(0.4-2)×10 ⁹	400-1900	1.5×10 ²⁰
RHR → OHR + H ₂ O + H ₂	(1-6)×10 ⁹	100-600	0.5×10 ²⁰
MAR + H ₂ O → OHR + H ₂	(1-6)×10 ⁹	100-600	0.5×10 ²⁰

*See Table S8; †For (1-5)×10⁹ mol H₂ yr⁻¹ equivalent to 0.4-1.4% H₂ in the plume gas (Table 1); ‡The duration to react a mass of rock equal to 1% of the mass of the core (7×10¹⁷ kg; Table S9) at the calculated reaction rate; §For complete conversion of the reactant rock in the whole core.

The actual yield of H₂ from AAR oxidation to RHR should be similar to the theoretical yield (Table S10). This is because metallic iron is unstable in the presence of liquid water at sub-kbar pressures (81), and Enceladus' core does not appear to be dense enough to permit a large amount of AAR to be present (10). This establishes a lower limit of ~1.5×10²⁰ moles for the amount of H₂ generated by water-rock reactions. All of the metallic iron accreted by Enceladus could have been oxidized during past hydrothermal processing (81), or a small fraction may remain and is reacting today.

For the reactions in Table S10 with ferrous iron-bearing reactants, the actual yields could be lower than the theoretical yields because ferrous iron in the reactants can avoid oxidation to magnetite if ferrous iron-bearing minerals are stable under conditions in the core. Assuming that the oxidation of rock is irreversible, the progress of these reactions on a global scale can be envisioned to depend on the total amount of fluid cycled through the core; and geochemical factors such as temperature (2), and the abundances of carbonate and aluminum (87, 88). While it is a complex problem to predict the extent of reaction progress, revisiting the previous example provides insight into the robustness of ferrous iron oxidation as a source of H₂. If only 1% of the FeO component of rock were oxidized to Fe₃O₄, then the yield of H₂ would still be ~5×10¹⁷ moles, which is enough to sustain the observed release rate of H₂ for hundreds of millions of years (Table S10). Unless the extent of reaction progress is miniscule, ferrous iron oxidation can be a geologically significant source of H₂ on Enceladus.

4.3. Stored vs. actively produced H₂ from the core

We consider the possibility that the observed H₂ was produced previously, but has been stored in Enceladus' core. In this scenario, one can imagine that "old H₂" is being released perhaps episodically by transport through fractures that may form as a result of tidal stresses. Previously, we calculated a relatively short length scale for diffusion of H₂ through the core ($L \approx 10$ km; section 4.2.3.2). If the core is impermeable, it could accumulate H₂ over time from organic pyrolysis (max yield = 3.5×10^{19} mol; section 4.2.1), pore water radiolysis (integrated yield over 4.56 Gyr = 3×10^{18} mol; section 4.2.3.2), or mineral oxidation (max yield = 2×10^{20} mol; section 4.2.5). These values imply that mineral oxidation has the greatest potential to provide H₂ for the plume. Decomposition of NH₃ could also contribute to the inventory of H₂ in the core, but this mechanism of H₂ production is inconsistent with the non-detection of N₂ in the plume (section 4.2.2).

As an initial attempt at addressing the question of whether H₂ in Enceladus' plume might come from seepage from a stored reservoir, we consider Kidd Creek mine in the Canadian Shield as a model for long-term storage of reduced gases in a water-rock system. Kidd Creek is chosen because it hosts fluids that have been trapped in fractured rocks for over a billion years [reported to be the oldest water on Earth; (89)], providing focus on the temporal aspect of the problem. These fluids have an H₂/CH₄ ratio of ~ 0.05 , which may reflect the consumption of H₂ during the abiotic synthesis of CH₄ (33). This process may be facilitated by the long timescale of water-rock interaction. The Enceladus plume has a much higher H₂/CH₄ ratio (~ 1 -14; Table 1), which suggests that the input of stored H₂ to the plume should be minimal if Kidd Creek fluids are applicable as terrestrial geochemical analogues of stored gas on Enceladus. Kidd Creek exemplifies the concept that fluids stored in rocks for long durations should have low H₂/CH₄ ratios. This notion is also supported by the lack of geochemical evidence for the active synthesis of CH₄ at hydrothermal vents (90), where the timescale of water-rock interaction during fluid circulation may be too short to allow appreciable synthesis of CH₄.

Kidd Creek can be considered an analogue that provides useful insight rather than an exact match for the core of Enceladus. Indeed, Enceladus' core is likely to be compositionally different from Kidd Creek because of their different geochemical histories. On the other hand, probable greater abundances of both carbon reactants [e.g., carbonate minerals and organic matter, as in carbonaceous chondrites and comets; (60, 91)] and transition metal catalysts of carbon hydrogenation [e.g., metallic nickel; (92, 93)] may enhance CH₄ synthesis while fluids are stored in the core. Given these factors, it seems unlikely that similarly aged fluids on Enceladus would have a higher H₂/CH₄ ratio than the Kidd Creek value [~ 0.05 ; (33)], which could be considered a provisional upper limit for Enceladus. While circumstantial, this argument bolsters the view that the majority of H₂ in the plume does not derive from a stored reservoir in the core, although the existence of such a reservoir is not to be excluded.

For a Kidd Creek-like gas to be a major contributor of H₂ to the plume, a second source or process inside Enceladus that increases the H₂/CH₄ ratio by adding H₂ or removing CH₄ would need to be invoked. For the case of H₂ addition, we can set an upper limit on the contribution of H₂ to the plume by assuming that all of the CH₄ in the plume is derived from stored gas. For the lower limit of H₂/CH₄ ≈ 1 in the plume (Table

1), the corresponding upper limit on the contribution of Kidd Creek-like gas is only ~5% of the total observed H₂. Therefore, an added (e.g., mineral-derived) source of H₂ would have to be the dominant source of H₂ (see below). The H₂/CH₄ ratio could also be increased if CH₄ is physically or chemically removed from a source fluid prior to outgassing. Oxidative chemistry is unlikely to increase the H₂/CH₄ ratio because H₂ is more reactive than CH₄. Clathrate hydrates can preferentially remove CH₄ over H₂ from a fluid (22, 94), but the fugacity of CH₄ in Enceladus' ocean may be too low to allow CH₄ to be incorporated into clathrates if they are being formed. A CH₄ fugacity between ~20 μbar and ~0.01 bar is inferred (Table S11, section 5.1), which is more than three orders of magnitude below the saturation fugacity of CH₄ clathrate at 273 K [~24 bar; (22)]. Thus, clathrate formation is unlikely to serve as a sink of CH₄. We conclude that the H₂/CH₄ ratio of the plume does not support a stored reservoir in Enceladus' core as a primary source of H₂ for the plume.

In contrast, there are many possible scenarios involving active production of H₂ in Enceladus' rocky core that could explain the H₂/CH₄ ratio in the plume. Let us consider a case where H₂ is being produced by hydrothermal processing of rocks (13) resembling carbonaceous chondrites or refractory cometary material. In this case, both organic pyrolysis and mineral oxidation can be robust sources of H₂ (sections 4.2.1 and 4.2.5). Pore water radiolysis may play a minor role but is disregarded here to simplify the discussion (section 4.2.3.2). Because minerals and organics are likely to be intermixed in these types of rocks, an H₂/CH₄ ratio derived from them could reflect contributions from both sources, depending on the current state of these materials and the conditions (e.g., temperature) to which they are subjected. To illustrate the concept of the plume as a mixture, we assume that fluid-mineral reactions yield H₂/CH₄ → ∞ (pure H₂ endmember), consistent with kinetically inhibited synthesis of CH₄ over short timescales (95). We further assume H₂/CH₄ ≈ 1 as a representative value for organic pyrolysis, based on stepwise heating experiments of Murchison IOM (57). Also, one can envision the existence of additional sources (perhaps spatially separated) that provide low H₂/CH₄ ratios (e.g., ~0 as an endmember) to the mixture before it erupts to produce the plume. This category may include clathrate hydrates in the ice shell (section 4.1.2), CH₄-rich fluids stored in the rocky core (see above), or methanogenic microorganisms (17).

The proposed mixing model does not provide a solution that uniquely satisfies the observed H₂/CH₄ ratio ≈ 1-14 (Table 1), because the system is underdetermined based on present data. However, it can be deduced that there is a large range of circumstances under which active production of H₂ can achieve consistency with the observational constraint (e.g., ~80% of the H₂ from mineral oxidation and ~20% from organic pyrolysis). Two additional general inferences are that organic pyrolysis by itself may be sufficient if H₂/CH₄ ≈ 1; or input of H₂ from mineral oxidation may be required if H₂/CH₄ > 1. It is notable that high H₂/CH₄ ratios are characteristic of fluids derived from active hydrothermal processing of ultramafic rocks on Earth, such as at Lost City where H₂/CH₄ ≈ 9 (34), although the geophysical setting of this activity (e.g., plate tectonics) is fundamentally different from Enceladus.

The hypothesis of active production of H₂ in the core of Enceladus can be consistent with the H₂/CH₄ ratio in the plume. A mixing model may be necessary, but this is not a great demand to place on a geologically active body, where mixing may be unavoidable [as in hydrothermal vent fluids on Earth; (90)]. Contrast this state of affairs

with the above model of stored H₂, for which there is no apparent and non-contrived way to reconcile the H₂/CH₄ ratio. Overall, this analysis favors actively produced over stored H₂ to explain the observations of H₂, because the latter appears inconsistent with the H₂/CH₄ ratio in the plume, whereas the former permits consistent possibilities in terms of plausible processes.

5. Thermodynamic analysis of volatile species

5.1. A model for ocean composition from the plume

Our goal is to develop a model that allows the dissolved gas composition of Enceladus' ocean to be estimated from the abundances of gases in the plume. We focus on CO₂, CH₄, and H₂ because they are key to quantifying the degree of disequilibrium between CO₂-CH₄. It is assumed that the proportions of these species in the plume gas are the same as in ocean water. This assumption requires minimal fractionation among these species during the outgassing process from ocean to plume (see below). The ratios of concentrations in the ocean are taken to be equal to the ratios of number densities of CH₄/CO₂ \approx 0.4 and H₂/CO₂ \approx 1.6 in the plume (Table 1). To convert such ratios to concentrations, we require the absolute concentration of one species in Enceladus' ocean. Previously, (15) used H₂O as the reference species for the fugacity, but this required them to try to account for a large amount of H₂O condensation that occurs during the outgassing process. Here, we adopt CO₂ as the reference species because it is much less condensable than H₂O, and more similar in volatility to CH₄ and H₂. Another reason why CO₂ is a useful choice is because its absolute concentration can be constrained, by linking it to independent measurements of carbonate species in plume particles via carbonate equilibria in Enceladus' ocean. We are not aware of any alternative approaches that could provide a more robust means of estimating the dissolved gas composition of Enceladus' ocean from plume gas measurements.

The concentration of CO₂ in Enceladus' ocean can be estimated using the carbonate speciation model of (15). Based on the composition of salt-rich plume particles (25, 26), we consider the ocean to have a nominal composition of \sim 0.1 mol of chloride and \sim 0.03 mol of total dissolved carbonate (TDC = HCO₃⁻ + CO₃⁻²) per kg of water, with Na⁺ as the most abundant cation. Our perspective is that a pH range of 9 to 11 provides the best compromise between published estimates [see Table 1 in (15)]. This is taken to be a nominal range rather than hard limits, but one can also consider the implications on the degree of disequilibrium between CO₂-CH₄ for lower and higher pH values in Fig. 4. The pH is the key source of potential uncertainty.

The concentration of CO₂ in the ocean is computed for a combination of Cl-TDC-pH using the model of (15). The concentrations of CH₄ and H₂ are obtained by scaling the concentration of CO₂ by the CH₄/CO₂ or H₂/CO₂ ratio in the plume. We assume an ideal dilute solution such that the activities of CO₂, CH₄, and H₂ are approximately equal to their molal concentrations. The fugacities of these species are computed using Henry's law constants (96, 97). The results of the geochemical calculations are given in Table S11. They are referred to as apparent quantities because they are derived from modeling of plume data, rather than directly measured in the ocean.

Table S11. Volatile composition of the ocean source of Enceladus’ plume. Apparent molal (mol kg⁻¹ of H₂O) concentrations (~activities) and fugacities of key volatile species are provided for nominal ocean composition models with a pH of 9 or 11 at 273 K and 1 bar. TDC refers to total dissolved carbonate.

Ocean model:	0.1 mol Cl ⁻ , 0.03 mol TDC, 1 kg H ₂ O, pH 9		0.1 mol Cl ⁻ , 0.03 mol TDC, 1 kg H ₂ O, pH 11	
Species	Molality/ Activity	Fugacity (bar)	Molality/ Activity	Fugacity (bar)
CO ₂	7×10 ⁻⁵	9×10 ⁻⁴	1×10 ⁻⁷	1×10 ⁻⁶
CH ₄	3×10 ⁻⁵	1×10 ⁻²	4×10 ⁻⁸	2×10 ⁻⁵
H ₂	1×10 ⁻⁴	1×10 ⁻¹	2×10 ⁻⁷	2×10 ⁻⁴

More generally, the molality of CO₂ in Enceladus’ ocean from our geochemical model can be expressed as a function of pH via

$$\log m_{CO_2} = -0.1213 \times (\text{pH})^2 + 0.9832 \times (\text{pH}) - 3.1741, \quad (\text{S18})$$

which reproduces the numerically calculated values to within an accuracy of ~20% from pH 7-14. This equation can be used to obtain approximate values for the molalities of CH₄ and H₂ in the ocean by multiplying the molality of CO₂ times the CH₄/CO₂ or H₂/CO₂ ratio in the plume, based on the assumption that these ratios are not significantly modified between ocean and plume (see below). In general, our model indicates that unlike the plume (Table 1), the ocean may be dilute in volatile gases with respect to H₂O, because condensation of H₂O during transport through the cold crust of Enceladus enriches the residual gas in volatiles (15).

Is it reasonable to assume that volatile ratios in the plume are similar to those in the ocean? This seems like a useful step in starting to explore the implications of the INMS measurements for ocean chemistry, but we can envision several processes that might result in volatile fractionation. First, ocean-derived CO₂ (the reference species in our model) could be removed from the gas by condensation. Some CO₂ probably condenses because spectroscopic signatures of CO₂ ices are reported in the tiger stripes (51). This suggests that the derived quantities for CH₄ and H₂ in the ocean are upper limits, because the ratios of CH₄/CO₂ and H₂/CO₂ in the ocean (with more CO₂) are lower than in the plume. However, chemical affinities depend on logarithmic abundances (section 5.2), so this effect may not be significant unless a very large amount (e.g., >99%) of ocean-derived CO₂ condenses.

Another possibility is that there could be non-ocean sources of CO₂ and CH₄, such as dry ice or clathrate hydrates in the ice shell of Enceladus, which contribute to the plume (54). The present data are ambivalent regarding the existence of such contributors to the plume. If there is an icy source of CO₂, then the derived quantities for CH₄ and H₂ in the ocean would be lower limits (the ocean could be richer in CH₄ and H₂ than calculated). On the other hand, the ocean may be poorer in CH₄ than calculated if there is an icy source of CH₄ for the plume. If there is an icy source providing both CO₂ and CH₄, then the derived quantities for H₂ in the ocean would still be lower limits, but it is not possible to determine the effect on the inferred abundance of CH₄ in the ocean without

information on the CH₄/CO₂ ratio from the icy source, and the relative contributions of icy and ocean sources for the plume. However, icy sources would need to be by far the dominant sources of CO₂ or CH₄ to have a significant impact on calculations of chemical affinity, owing to the logarithmic dependence on species abundances (section 5.2). Given the above possible competing effects stemming from data limitations, it seems apt to preface the derived quantities with the term apparent in recognition of the uncertainties.

We also address if volatiles could be fractionated during degassing from ocean water. Would the proportions of degassed volatiles that go into the plume be similar to the proportions originally dissolved in ocean water? This is a kinetic problem, as the presence of salts in plume particles demonstrate flash freezing of liquid water droplets in the eruption zone (25, 26). To determine if volatile fractionation occurs, we need to compare the freezing timescale to the timescales for processes that fractionate volatiles as droplets degas and freeze.

We begin by making an estimate of the freezing time for droplets of ocean water that are evaporatively cooled in the subsurface (98). From kinetic gas theory, the net evaporative flux (J) of H₂O can be evaluated using the Hertz-Knudsen equation

$$J = \Delta P \left(\frac{M}{2\pi RT} \right)^{1/2}, \quad (\text{S19})$$

where ΔP designates the difference between the saturation vapor pressure and the ambient pressure of H₂O, $M = 0.018 \text{ kg mol}^{-1}$, $R = 8.3 \text{ J mol}^{-1} \text{ K}^{-1}$, and $T = 273 \text{ K}$. Taking ΔP to be of order 1 mbar (100 Pa), we obtain $J \approx 0.1 \text{ kg m}^{-2} \text{ s}^{-1}$.

The evaporation rate from spherical droplets with radii of order 1 μm (26) is calculated to be $\sim 1 \times 10^{-12} \text{ kg s}^{-1}$ (based on the surface area of the droplets). Because the heat of vaporization of water is approximately 10 times larger than the heat of fusion, about 10% of a droplet's mass will be evaporated, which results in an evaporated mass of $\sim 4 \times 10^{-16} \text{ kg}$ per droplet. Using this mass and the calculated evaporation rate, we compute that it would take $\sim 0.4 \text{ ms}$ for a droplet to freeze. Informed by this result, below we consider a nominal freezing time of $\sim 1 \text{ ms}$.

We investigate whether CO₂, CH₄, and H₂ could be physically fractionated as these species, which are initially dissolved in ocean water, diffuse through water droplets erupted from the ocean. A characteristic length for diffusion in one-dimension can be written as

$$\delta \approx (D\tau)^{1/2}, \quad (\text{S20})$$

where D denotes the diffusion coefficient of the species of interest in liquid water at 0°C, and τ the freezing time. Equation S20 can be evaluated by adopting the following representative values for the parameters: $D_{\text{CO}_2} \approx 0.9 \mu\text{m}^2 \text{ ms}^{-1}$, $D_{\text{CH}_4} \approx 0.9 \mu\text{m}^2 \text{ ms}^{-1}$, $D_{\text{H}_2} \approx 2.8 \mu\text{m}^2 \text{ ms}^{-1}$ (99), and $\tau \approx 1 \text{ ms}$ (see above). The diffusive length scales are calculated to be: $\delta_{\text{CO}_2} \approx 0.9 \mu\text{m}$, $\delta_{\text{CH}_4} \approx 0.9 \mu\text{m}$, and $\delta_{\text{H}_2} \approx 1.7 \mu\text{m}$. These distances are comparable to the canonical droplet radius of $\sim 1 \mu\text{m}$. Therefore, the droplets can be expected to be significantly but not completely degassed of CO₂, CH₄, and H₂ before freezing.

The relationship in Eq. S20 can be used to set an upper limit on the magnitude of fractionation between gases that diffuse out of droplets, and the initial composition of droplets prior to degassing. For an endmember of limited degassing, the ratio of species X to CO₂ in the degassed fraction is approximately related to the original ocean water ratio by

$$\left(\text{X}/\text{CO}_2\right)_{\text{degas}} \approx \left(D_X / D_{\text{CO}_2}\right)^{1/2} \left(\text{X}/\text{CO}_2\right)_0. \quad (\text{S21})$$

Evaluations of this expression show that diffusion should not fractionate CO₂ and CH₄, while differential rates of diffusion can enrich the degassed fraction in H₂/CO₂ by no more than a factor of ~2. However, this value corresponds to an upper limit because more degassing would decrease the magnitude of the fractionation towards the limit of no fractionation for complete degassing. We conclude that a small amount of diffusive fractionation could be occurring during the degassing process, but it can be expected to be insignificant compared to the much larger effect of pH (e.g., Table S11).

Next, we consider if the conversion of HCO₃⁻ or CO₃⁻² to CO₂ during degassing from liquid water droplets could fractionate the ratios of CH₄/CO₂ and H₂/CO₂ between a source fluid and the resulting gas. This would add CO₂ to the gas that our model does not take into account, and the removal of carbonate-derived CO₂ would increase the pH in the droplets via CO₂-producing reactions such as



although the increased pH would inhibit further degassing of CO₂. It is general knowledge in geochemistry that CO₂ production from carbonate species is rapid but not instantaneous. Could this process contribute extra CO₂ to the plume, based on the relevant timescales on Enceladus?

We constrain the timescale for the chemical production of CO₂ using laboratory rate data reported by (100) that quantify the kinetics of CO₂ formation from carbonate species. The rate of carbonate species conversion to CO₂ can be expressed as

$$-\frac{d[\text{TDC}]}{dt} = k_{\text{eff}}[\text{HCO}_3^-], \quad (\text{S23})$$

where brackets are used to indicate the molar concentration of the enclosed species, t represents the duration of the conversion process, and the effective rate constant is given by

$$k_{\text{eff}} = k_d a_{\text{H}^+} + k_{\text{HCO}_3^-}, \quad (\text{S24})$$

where a_{H^+} stands for the activity of H⁺. We have adopted the notation of (100) for the rate constants k_d and $k_{\text{HCO}_3^-}$. Based on the data of (100), we use representative values of $k_d \approx 4 \times 10^3 \text{ L mol}^{-1} \text{ s}^{-1}$ and $k_{\text{HCO}_3^-} \approx 1 \times 10^{-5} \text{ s}^{-1}$ at 0°C. Because there seems to be general agreement that the Enceladus ocean has a pH > 9 [see Table 1 in (15)], the first term in Eq. S24 is insignificant compared to the second one, and the rate is governed by $k_{\text{HCO}_3^-}$.

and generally not sensitive to pH. The chemical lifetime (*e*-folding time) for CO₂ production from carbonate species can be calculated as $\tau_{chem} = k_{eff}^{-1} \approx 30$ h. Because this is much longer than the estimated freezing time (~1 ms), it is evident that there is not enough time for carbonate species to convert to CO₂ that contributes to the plume. There should not be appreciable chemical fractionation between CO₂ and other volatiles during degassing, because dissolved CO₂ is the only source of CO₂ for the plume from the ocean. Degassing of this CO₂ will not cause a pH increase, because only degassing of carbonate-derived CO₂ removes negative charge from the solution that must be balanced by a pH increase (e.g., Eq. S22).

5.2. Chemical affinity for methanogenesis in the ocean

We calculate the chemical affinity for CH₄ formation from CO₂ (methanogenesis, abiotic or biotic) in Enceladus' ocean using standard state thermodynamic data, and geochemical data from Enceladus. The chemical affinity (*A*) of a reaction is defined as the negative of the change in Gibbs energy with respect to the progress of the reaction (101). Thermodynamically favorable reactions have positive affinities, unfavorable ones have negative affinities, and reactions at equilibrium have zero affinity. In this work, the standard states are the ideal gas at 1 bar and any temperature, a hypothetical one molal solution referenced to infinite dilution at any temperature and pressure, and pure liquid water at any temperature and pressure (96, 97).

A net reaction for H₂-driven methanogenesis can be written as



and the affinity for this reaction can be computed via

$$A = 2.3026RT (\log K - \log Q), \quad (\text{S26})$$

where *R* stands for the gas constant (8.31446 J mol⁻¹ K⁻¹), *T* the temperature of the system (taken to be an ocean temperature of 273 K), *K* the equilibrium constant (dependent on the temperature and pressure of the system), and *Q* the reaction quotient (dependent on the composition of the system). The equilibrium constant at 273 K and 1 bar (log *K* = 37.44) is computed using the geochemical thermodynamics program SUPCRT92 (102). The pressure dependence is neglected here because it is negligible for the case of Enceladus' ocean (e.g., Δlog *K* = 0.1 from 1 to 100 bar). The equilibrium constant for Rxn. S25 is only weakly dependent on total pressure (*P*) because the change in standard volume (Δ*V*^o) for the reaction is small [-50 cm³ mol⁻¹ at 273 K and 1 bar; (102)]. Because Δ*V*^o is approximately constant with total pressure between 1 and 100 bar, log *K* varies linearly with total pressure between 1 and 100 bar (102). This linear relationship can be extrapolated to obtain log *K* at zero pressure, which to two decimal places is found to be identical to the value at 1 bar. This type of weak pressure dependence is a general feature of solution-phase reactions because of the effect of volume

$$\left(\frac{\partial \ln K}{\partial P}\right)_T = -\frac{\Delta V^\circ}{RT}. \quad (\text{S27})$$

The reaction quotient for Rxn. S25 can be expressed as

$$\log Q = \log a_{\text{CH}_4} + 2\log a_{\text{H}_2\text{O}} - \log a_{\text{CO}_2} - 4\log a_{\text{H}_2}, \quad (\text{S28})$$

where a_i represents the activity of the indicated aqueous species. A species in its standard state has an activity of unity by definition. To obtain the required activities, we use the geochemical model described in section 5.1. The model indicates that the activity of H_2O should not be less than 0.99 (dimensionless by convention), so this activity can be approximated as unity. Values for the other activities are obtained from the model (e.g., Table S11). Once the reaction quotient is computed, Eq. S26 can be evaluated to calculate the apparent affinity for methanogenesis in Enceladus' ocean (see Fig. 4).

References

1. N. H. Sleep, A. Meibom, T. Fridriksson, R. G. Coleman, D. K. Bird, H₂-rich fluids from serpentinization: Geochemical and biotic implications. *Proc. Natl. Acad. Sci. U.S.A.* **101**, 12818–12823 (2004). [doi:10.1073/pnas.0405289101](https://doi.org/10.1073/pnas.0405289101) [Medline](#)
2. T. M. McCollom, W. Bach, Thermodynamic constraints on hydrogen generation during serpentinization of ultramafic rocks. *Geochim. Cosmochim. Acta* **73**, 856–875 (2009). [doi:10.1016/j.gca.2008.10.032](https://doi.org/10.1016/j.gca.2008.10.032)
3. E. Shock, P. Canovas, The potential for abiotic organic synthesis and biosynthesis at seafloor hydrothermal systems. *Geofluids* **10**, 161 (2010). [doi:10.1111/j.1468-8123.2010.00277.x](https://doi.org/10.1111/j.1468-8123.2010.00277.x)
4. J. P. Amend, T. M. McCollom, M. Hentscher, W. Bach, Catabolic and anabolic energy for chemolithoautotrophs in deep-sea hydrothermal systems hosted in different rock types. *Geochim. Cosmochim. Acta* **75**, 5736–5748 (2011). [doi:10.1016/j.gca.2011.07.041](https://doi.org/10.1016/j.gca.2011.07.041)
5. K. Raymann, C. Brochier-Armanet, S. Gribaldo, The two-domain tree of life is linked to a new root for the Archaea. *Proc. Natl. Acad. Sci. U.S.A.* **112**, 6670–6675 (2015). [doi:10.1073/pnas.1420858112](https://doi.org/10.1073/pnas.1420858112) [Medline](#)
6. J. B. Corliss, J. Dymond, L. I. Gordon, J. M. Edmond, R. P. von Herzen, R. D. Ballard, K. Green, D. Williams, A. Bainbridge, K. Crane, T. H. van Andel, Submarine thermal springs on the galapagos rift. *Science* **203**, 1073–1083 (1979). [doi:10.1126/science.203.4385.1073](https://doi.org/10.1126/science.203.4385.1073) [Medline](#)
7. D. S. Kelley, J. A. Karson, D. K. Blackman, G. L. Früh-Green, D. A. Butterfield, M. D. Lilley, E. J. Olson, M. O. Schrenk, K. K. Roe, G. T. Lebon, P. Rivizzigno, An off-axis hydrothermal vent field near the Mid-Atlantic Ridge at 30°N. *Nature* **412**, 145–149 (2001). [doi:10.1038/35084000](https://doi.org/10.1038/35084000) [Medline](#)
8. D. S. Kelley, J. A. Karson, G. L. Früh-Green, D. R. Yoerger, T. M. Shank, D. A. Butterfield, J. M. Hayes, M. O. Schrenk, E. J. Olson, G. Proskurowski, M. Jakuba, A. Bradley, B. Larson, K. Ludwig, D. Glickson, K. Buckman, A. S. Bradley, W. J. Brazelton, K. Roe, M. J. Elend, A. Delacour, S. M. Bernasconi, M. D. Lilley, J. A. Baross, R. E. Summons, S. P. Sylva, A serpentinite-hosted ecosystem: The Lost City hydrothermal field. *Science* **307**, 1428–1434 (2005). [doi:10.1126/science.1102556](https://doi.org/10.1126/science.1102556) [Medline](#)
9. L. Iess, D. J. Stevenson, M. Parisi, D. Hemingway, R. A. Jacobson, J. I. Lunine, F. Nimmo, J. W. Armstrong, S. W. Asmar, M. Ducci, P. Tortora, The gravity field and interior structure of Enceladus. *Science* **344**, 78–80 (2014). [doi:10.1126/science.1250551](https://doi.org/10.1126/science.1250551) [Medline](#)
10. W. B. McKinnon, Effect of Enceladus's rapid synchronous spin on interpretation of Cassini gravity. *Geophys. Res. Lett.* **42**, 2137–2143 (2015). [doi:10.1002/2015GL063384](https://doi.org/10.1002/2015GL063384)

11. P. C. Thomas, R. Tajeddine, M. S. Tiscareno, J. A. Burns, J. Joseph, T. J. Lored, P. Helfenstein, C. Porco, Enceladus's measured physical libration requires a global subsurface ocean. *Icarus* **264**, 37–47 (2016). [doi:10.1016/j.icarus.2015.08.037](https://doi.org/10.1016/j.icarus.2015.08.037)
12. O. Čadež, G. Tobie, T. Van Hoolst, M. Massé, G. Choblet, A. Lefèvre, G. Mitri, R.-M. Baland, M. Běhouňková, O. Bourgeois, A. Trinh, Enceladus's internal ocean and ice shell constrained from Cassini gravity, shape, and libration data. *Geophys. Res. Lett.* **43**, 5653–5660 (2016). [doi:10.1002/2016GL068634](https://doi.org/10.1002/2016GL068634)
13. H.-W. Hsu, F. Postberg, Y. Sekine, T. Shibuya, S. Kempf, M. Horányi, A. Juhász, N. Altobelli, K. Suzuki, Y. Masaki, T. Kuwatani, S. Tachibana, S. I. Sirono, G. Moragas-Klostermeyer, R. Srama, Ongoing hydrothermal activities within Enceladus. *Nature* **519**, 207–210 (2015). [doi:10.1038/nature14262](https://doi.org/10.1038/nature14262) [Medline](#)
14. J. H. Waite Jr., M. R. Combi, W. H. Ip, T. E. Cravens, R. L. McNutt Jr., W. Kasprzak, R. Yelle, J. Luhmann, H. Niemann, D. Gell, B. Magee, G. Fletcher, J. Lunine, W. L. Tseng, Cassini ion and neutral mass spectrometer: Enceladus plume composition and structure. *Science* **311**, 1419–1422 (2006). [doi:10.1126/science.1121290](https://doi.org/10.1126/science.1121290) [Medline](#)
15. C. R. Glein, J. A. Baross, J. H. Waite Jr., The pH of Enceladus' ocean. *Geochim. Cosmochim. Acta* **162**, 202–219 (2015). [doi:10.1016/j.gca.2015.04.017](https://doi.org/10.1016/j.gca.2015.04.017)
16. Y. Sekine, T. Shibuya, F. Postberg, H.-W. Hsu, K. Suzuki, Y. Masaki, T. Kuwatani, M. Mori, P. K. Hong, M. Yoshizaki, S. Tachibana, S. I. Sirono, High-temperature water-rock interactions and hydrothermal environments in the chondrite-like core of Enceladus. *Nat. Commun.* **6**, 8604 (2015). [doi:10.1038/ncomms9604](https://doi.org/10.1038/ncomms9604) [Medline](#)
17. C. P. McKay, C. C. Porco, T. Altheide, W. L. Davis, T. A. Kral, The possible origin and persistence of life on Enceladus and detection of biomarkers in the plume. *Astrobiology* **8**, 909–919 (2008). [doi:10.1089/ast.2008.0265](https://doi.org/10.1089/ast.2008.0265) [Medline](#)
18. J. H. Waite Jr., W. S. Lewis, W. T. Kasprzak, V. G. Anicich, B. P. Block, T. E. Cravens, G. G. Fletcher, W.-H. Ip, J. G. Luhmann, R. L. McNutt, H. B. Niemann, J. K. Parejko, J. E. Richards, R. L. Thorpe, E. M. Walter, R. V. Yelle, The Cassini Ion and Neutral Mass Spectrometer (INMS) investigation. *Space Sci. Rev.* **114**, 113–231 (2004). [doi:10.1007/s11214-004-1408-2](https://doi.org/10.1007/s11214-004-1408-2)
19. J. H. Waite Jr., W. S. Lewis, B. A. Magee, J. I. Lunine, W. B. McKinnon, C. R. Glein, O. Mousis, D. T. Young, T. Brockwell, J. Westlake, M.-J. Nguyen, B. D. Teolis, H. B. Niemann, R. L. McNutt, M. Perry, W.-H. Ip, Liquid water on Enceladus from observations of ammonia and ⁴⁰Ar in the plume. *Nature* **460**, 487–490 (2009). [doi:10.1038/nature08153](https://doi.org/10.1038/nature08153)
20. See supplementary materials.
21. B. D. Teolis, H. B. Niemann, J. H. Waite, D. A. Gell, R. S. Perryman, W. T. Kasprzak, K. E. Mandt, R. V. Yelle, A. Y. Lee, F. J. Pelletier, G. P. Miller, D. T. Young, J. M. Bell, B. A.

- Magee, E. L. Patrick, J. Grimes, G. G. Fletcher, V. Vuitton, A revised sensitivity model for Cassini INMS: Results at Titan. *Space Sci. Rev.* **190**, 47–84 (2015). [doi:10.1007/s11214-014-0133-8](https://doi.org/10.1007/s11214-014-0133-8)
22. J. I. Lunine, D. J. Stevenson, Thermodynamics of clathrate hydrate at low and high pressures with application to the outer solar system. *Astrophys. J. Suppl. Ser.* **58**, 493 (1985). [doi:10.1086/191050](https://doi.org/10.1086/191050)
23. W. L. Mao, H. K. Mao, Hydrogen storage in molecular compounds. *Proc. Natl. Acad. Sci. U.S.A.* **101**, 708–710 (2004). [doi:10.1073/pnas.0307449100](https://doi.org/10.1073/pnas.0307449100) [Medline](#)
24. C. J. Hansen, D. E. Shemansky, L. W. Esposito, A. I. F. Stewart, B. R. Lewis, J. E. Colwell, A. R. Hendrix, R. A. West, J. H. Waite Jr., B. Teolis, B. A. Magee, The composition and structure of the Enceladus plume. *Geophys. Res. Lett.* **38**, L11202 (2011). [doi:10.1029/2011GL047415](https://doi.org/10.1029/2011GL047415)
25. F. Postberg, S. Kempf, J. Schmidt, N. Brilliantov, A. Beinsen, B. Abel, U. Buck, R. Srama, Sodium salts in E-ring ice grains from an ocean below the surface of Enceladus. *Nature* **459**, 1098–1101 (2009). [doi:10.1038/nature08046](https://doi.org/10.1038/nature08046) [Medline](#)
26. F. Postberg, J. Schmidt, J. Hillier, S. Kempf, R. Srama, A salt-water reservoir as the source of a compositionally stratified plume on Enceladus. *Nature* **474**, 620–622 (2011). [doi:10.1038/nature10175](https://doi.org/10.1038/nature10175) [Medline](#)
27. C. R. Glein, E. L. Shock, Sodium chloride as a geophysical probe of a subsurface ocean on Enceladus. *Geophys. Res. Lett.* **37**, L09204 (2010). [doi:10.1029/2010GL042446](https://doi.org/10.1029/2010GL042446)
28. H. Balsiger, K. Altwegg, A. Bar-Nun, J.-J. Berthelier, A. Bieler, P. Bochslers, C. Briois, U. Calmonte, M. Combi, J. De Keyser, P. Eberhardt, B. Fiethe, S. A. Fuselier, S. Gasc, T. I. Gombosi, K. C. Hansen, M. Hässig, A. Jäckel, E. Kopp, A. Korth, L. Le Roy, U. Mall, B. Marty, O. Mousis, T. Owen, H. Rème, M. Rubin, T. Sémon, C.-Y. Tzou, J. H. Waite, P. Wurz, Detection of argon in the coma of comet 67P/Churyumov-Gerasimenko. *Sci. Adv.* **1**, e1500377 (2015). [doi:10.1126/sciadv.1500377](https://doi.org/10.1126/sciadv.1500377) [Medline](#)
29. A. Bar-Nun, D. Prialnik, The possible formation of a hydrogen coma around comets at large heliocentric distances. *Astrophys. J.* **324**, L31–L34 (1988). [doi:10.1086/185084](https://doi.org/10.1086/185084) [Medline](#)
30. J. Telling, E. S. Boyd, N. Bone, E. L. Jones, M. Tranter, J. W. MacFarlane, P. G. Martin, J. L. Wadham, G. Lamarche-Gagnon, M. L. Skidmore, T. L. Hamilton, E. Hill, M. Jackson, D. A. Hodgson, Rock comminution as a source of hydrogen for subglacial ecosystems. *Nat. Geosci.* **8**, 851–855 (2015). [doi:10.1038/ngeo2533](https://doi.org/10.1038/ngeo2533)
31. B. Sherwood Lollar, T. C. Onstott, G. Lacrampe-Couloume, C. J. Ballentine, The contribution of the Precambrian continental lithosphere to global H₂ production. *Nature* **516**, 379–382 (2014). [doi:10.1038/nature14017](https://doi.org/10.1038/nature14017) [Medline](#)

32. C. C. Blair, S. D'Hondt, A. J. Spivack, R. H. Kingsley, Radiolytic hydrogen and microbial respiration in subsurface sediments. *Astrobiology* **7**, 951–970 (2007). [doi:10.1089/ast.2007.0150](https://doi.org/10.1089/ast.2007.0150) [Medline](#)
33. B. Sherwood Lollar, T. D. Westgate, J. A. Ward, G. F. Slater, G. Lacrampe-Couloume, Abiogenic formation of alkanes in the Earth's crust as a minor source for global hydrocarbon reservoirs. *Nature* **416**, 522–524 (2002). [doi:10.1038/416522a](https://doi.org/10.1038/416522a) [Medline](#)
34. G. Proskurowski, M. D. Lilley, D. S. Kelley, E. J. Olson, Low temperature volatile production at the Lost City Hydrothermal Field, evidence from a hydrogen stable isotope geothermometer. *Chem. Geol.* **229**, 331–343 (2006). [doi:10.1016/j.chemgeo.2005.11.005](https://doi.org/10.1016/j.chemgeo.2005.11.005)
35. J. H. Roberts, The fluffy core of Enceladus. *Icarus* **258**, 54–66 (2015). [doi:10.1016/j.icarus.2015.05.033](https://doi.org/10.1016/j.icarus.2015.05.033)
36. B. J. Travis, G. Schubert, Keeping Enceladus warm. *Icarus* **250**, 32–42 (2015). [doi:10.1016/j.icarus.2014.11.017](https://doi.org/10.1016/j.icarus.2014.11.017)
37. J. W. McConkey, C. P. Malone, P. V. Johnson, C. Winstead, V. McKoy, I. Kanik, Electron impact dissociation of oxygen-containing molecules—A critical review. *Phys. Rep.* **466**, 1–103 (2008). [doi:10.1016/j.physrep.2008.05.001](https://doi.org/10.1016/j.physrep.2008.05.001)
38. B. D. Teolis, M. E. Perry, B. A. Magee, J. Westlake, J. H. Waite, Detection and measurement of ice grains and gas distribution in the Enceladus plume by Cassini's Ion Neutral Mass Spectrometer. *J. Geophys. Res.* **115**, A09222 (2010). [doi:10.1029/2009JA015192](https://doi.org/10.1029/2009JA015192)
39. M. E. Perry, B. D. Teolis, H. T. Smith, R. L. McNutt Jr., G. Fletcher, W. Kasprzak, B. Magee, D. G. Mitchell, J. H. Waite Jr., Cassini INMS observations of neutral molecules in Saturn's E-ring. *J. Geophys. Res.* **115**, A10206 (2010). [doi:10.1029/2010JA015248](https://doi.org/10.1029/2010JA015248)
40. D. A. Dahl, SIMION for the personal computer in reflection. *Int. J. Mass Spectrom.* **200**, 3–25 (2000). [doi:10.1016/S1387-3806\(00\)00305-5](https://doi.org/10.1016/S1387-3806(00)00305-5)
41. C. Porco, D. DiNino, F. Nimmo, How the geysers, tidal stresses, and thermal emission across the south polar terrain of Enceladus are related. *Astron. J.* **148**, 45 (2014). [doi:10.1088/0004-6256/148/3/45](https://doi.org/10.1088/0004-6256/148/3/45)
42. Y. Dong, T. W. Hill, B. D. Teolis, B. A. Magee, J. H. Waite, The water vapor plumes of Enceladus. *J. Geophys. Res.* **116**, A10204 (2011). [doi:10.1029/2011JA016693](https://doi.org/10.1029/2011JA016693)
43. C. J. Hansen, L. W. Esposito, A. I. F. Stewart, B. Meinke, B. Wallis, J. E. Colwell, A. R. Hendrix, K. Larsen, W. Pryor, F. Tian, Water vapour jets inside the plume of gas leaving Enceladus. *Nature* **456**, 477–479 (2008). [doi:10.1038/nature07542](https://doi.org/10.1038/nature07542) [Medline](#)
44. K. Lodders, Solar system abundances and condensation temperatures of the elements. *Astrophys. J.* **591**, 1220–1247 (2003). [doi:10.1086/375492](https://doi.org/10.1086/375492)

45. J. B. Pollack, O. Hubickyj, P. Bodenheimer, J. J. Lissauer, M. Podolak, Y. Greenzweig, Formation of the giant planets by concurrent accretion of solids and gas. *Icarus* **124**, 62–85 (1996). [doi:10.1006/icar.1996.0190](https://doi.org/10.1006/icar.1996.0190)
46. H. B. Niemann, S. K. Atreya, J. E. Demick, D. Gautier, J. A. Haberman, D. N. Harpold, W. T. Kasprzak, J. I. Lunine, T. C. Owen, F. Raulin, Composition of Titan's lower atmosphere and simple surface volatiles as measured by the Cassini-Huygens probe gas chromatograph mass spectrometer experiment. *J. Geophys. Res.* **115**, E12006 (2010). [doi:10.1029/2010JE003659](https://doi.org/10.1029/2010JE003659)
47. M. J. Mumma, S. B. Charnley, The chemical composition of comets—Emerging taxonomies and natal heritage. *Annu. Rev. Astron. Astrophys.* **49**, 471–524 (2011). [doi:10.1146/annurev-astro-081309-130811](https://doi.org/10.1146/annurev-astro-081309-130811)
48. M. Rubin, K. Altwegg, H. Balsiger, A. Bar-Nun, J.-J. Berthelier, A. Bieler, P. Bochsler, C. Briois, U. Calmonte, M. Combi, J. De Keyser, F. Dhooghe, P. Eberhardt, B. Fiethe, S. A. Fuselier, S. Gasc, T. I. Gombosi, K. C. Hansen, M. Hässig, A. Jäckel, E. Kopp, A. Korth, L. Le Roy, U. Mall, B. Marty, O. Mousis, T. Owen, H. Rème, T. Sémon, C.-Y. Tzou, J. H. Waite, P. Wurz, Molecular nitrogen in comet 67P/Churyumov-Gerasimenko indicates a low formation temperature. *Science* **348**, 232–235 (2015). [doi:10.1126/science.aaa6100](https://doi.org/10.1126/science.aaa6100) [Medline](#)
49. O. Mousis, J. I. Lunine, A. Luspay-Kuti, T. Guillot, B. Marty, M. Ali-Dib, P. Wurz, K. Altwegg, A. Bieler, M. Hässig, M. Rubin, P. Vernazza, J. H. Waite, A protosolar nebula origin for the ices agglomerated by comet 67P/Churyumov-Gerasimenko. *Astrophys. J.* **819**, L33 (2016). [doi:10.3847/2041-8205/819/2/L33](https://doi.org/10.3847/2041-8205/819/2/L33)
50. J. R. Spencer, J. C. Pearl, M. Segura, F. M. Flasar, A. Mamoutkine, P. Romani, B. J. Buratti, A. R. Hendrix, L. J. Spilker, R. M. Lopes, Cassini encounters Enceladus: Background and the discovery of a south polar hot spot. *Science* **311**, 1401–1405 (2006). [doi:10.1126/science.1121661](https://doi.org/10.1126/science.1121661) [Medline](#)
51. R. H. Brown, R. N. Clark, B. J. Buratti, D. P. Cruikshank, J. W. Barnes, R. M. Mastrapa, J. Bauer, S. Newman, T. Momary, K. H. Baines, G. Bellucci, F. Capaccioni, P. Cerroni, M. Combes, A. Coradini, P. Drossart, V. Formisano, R. Jaumann, Y. Langevin, D. L. Matson, T. B. McCord, R. M. Nelson, P. D. Nicholson, B. Sicardy, C. Sotin, Composition and physical properties of Enceladus' surface. *Science* **311**, 1425–1428 (2006). [doi:10.1126/science.1121031](https://doi.org/10.1126/science.1121031) [Medline](#)
52. X.-H. Wang, H.-B. Qin, A. Dandekar, Y.-F. Wang, Y.-F. Sun, Q.-L. Ma, B. Liu, L.-Y. Yang, C.-Y. Sun, G.-J. Chen, Hydrate phase equilibrium of H₂/CH₄/CO₂ ternary gas mixtures and cage occupancy percentage of hydrogen molecules. *Fluid Phase Equilib.* **403**, 160–166 (2015). [doi:10.1016/j.fluid.2015.06.020](https://doi.org/10.1016/j.fluid.2015.06.020)
53. E. D. Sloan, C. A. Koh, *Clathrate Hydrates of Natural Gases* (CRC Press, ed. 3, 2008).

54. S. W. Kieffer, X. Lu, C. M. Bethke, J. R. Spencer, S. Marshak, A. Navrotsky, A clathrate reservoir hypothesis for Enceladus' south polar plume. *Science* **314**, 1764–1766 (2006). [doi:10.1126/science.1133519](https://doi.org/10.1126/science.1133519) [Medline](#)
55. O. Mousis, J. I. Lunine, C. Thomas, M. Pasek, U. Marboeuf, Y. Alibert, V. Ballenegger, D. Cordier, Y. Ellinger, F. Pauzat, S. Picaud, Clathration of volatiles in the solar nebula and implications for the origin of Titan's atmosphere. *Astrophys. J.* **691**, 1780–1786 (2009). [doi:10.1088/0004-637X/691/2/1780](https://doi.org/10.1088/0004-637X/691/2/1780)
56. J. S. Lewis, R. G. Prinn, Kinetic inhibition of CO and N₂ reduction in the solar nebula. *Astrophys. J.* **238**, 357 (1980). [doi:10.1086/157992](https://doi.org/10.1086/157992)
57. F. Okumura, K. Mimura, Gradual and stepwise pyrolyses of insoluble organic matter from the Murchison meteorite revealing chemical structure and isotopic distribution. *Geochim. Cosmochim. Acta* **75**, 7063–7080 (2011). [doi:10.1016/j.gca.2011.09.015](https://doi.org/10.1016/j.gca.2011.09.015)
58. L. Remusat, S. Derenne, F. Robert, H. Knicker, New pyrolytic and spectroscopic data on Orgueil and Murchison insoluble organic matter: A different origin than soluble? *Geochim. Cosmochim. Acta* **69**, 3919–3932 (2005). [doi:10.1016/j.gca.2005.02.032](https://doi.org/10.1016/j.gca.2005.02.032)
59. C. M. O. D. Alexander, M. Fogel, H. Yabuta, G. D. Cody, The origin and evolution of chondrites recorded in the elemental and isotopic compositions of their macromolecular organic matter. *Geochim. Cosmochim. Acta* **71**, 4380–4403 (2007). [doi:10.1016/j.gca.2007.06.052](https://doi.org/10.1016/j.gca.2007.06.052)
60. J. Kissel, F. R. Krueger, The organic component in dust from comet Halley as measured by the PUMA mass spectrometer on board Vega 1. *Nature* **326**, 755–760 (1987). [doi:10.1038/326755a0](https://doi.org/10.1038/326755a0)
61. B. D. Teolis, G. H. Jones, P. F. Miles, R. L. Tokar, B. A. Magee, J. H. Waite, E. Roussos, D. T. Young, F. J. Crary, A. J. Coates, R. E. Johnson, W.-L. Tseng, R. A. Baragiola, Cassini finds an oxygen-carbon dioxide atmosphere at Saturn's icy moon Rhea. *Science* **330**, 1813–1815 (2010). [doi:10.1126/science.1198366](https://doi.org/10.1126/science.1198366) [Medline](#)
62. B. D. Teolis, J. H. Waite, Dione and Rhea seasonal exospheres revealed by Cassini CAPS and INMS. *Icarus* **272**, 277–289 (2016). [doi:10.1016/j.icarus.2016.02.031](https://doi.org/10.1016/j.icarus.2016.02.031)
63. B. A. Hofmann, in *Proceedings of the 7th International Symposium on Water-Rock Interaction*, Y. K. Kharaka, A. S. Maest, Eds. (Balkema, Park City, UT, 1992), pp. 503–506.
64. R. E. Harris, S. M. Pimblott, On ³H β-particle and ⁶⁰Co γ irradiation of aqueous systems. *Radiat. Res.* **158**, 493–504 (2002). [doi:10.1667/0033-7587\(2002\)158\[0493:OHPACI\]2.0.CO;2](https://doi.org/10.1667/0033-7587(2002)158[0493:OHPACI]2.0.CO;2) [Medline](#)
65. L.-H. Lin, G. F. Slater, B. Sherwood Lollar, G. Lacrampe-Couloume, T. C. Onstott, The yield and isotopic composition of radiolytic H₂, a potential energy source for the deep

- subsurface biosphere. *Geochim. Cosmochim. Acta* **69**, 893–903 (2005).
[doi:10.1016/j.gca.2004.07.032](https://doi.org/10.1016/j.gca.2004.07.032)
66. R. M. Hazen, R. C. Ewing, D. A. Sverjensky, Evolution of uranium and thorium minerals. *Am. Mineral.* **94**, 1293–1311 (2009). [doi:10.2138/am.2009.3208](https://doi.org/10.2138/am.2009.3208)
67. E. Jacobs, K. Wouters, G. Volckaert, H. Moors, N. Maes, C. Bruggeman, R. Swennen, R. Littke, Measuring the effective diffusion coefficient of dissolved hydrogen in saturated Boom Clay. *Appl. Geochem.* **61**, 175–184 (2015). [doi:10.1016/j.apgeochem.2015.05.022](https://doi.org/10.1016/j.apgeochem.2015.05.022)
68. P. A. Bland, M. D. Jackson, R. F. Coker, B. A. Cohen, J. B. W. Webber, M. R. Lee, C. M. Duffy, R. J. Chater, M. G. Ardakani, D. S. McPhail, D. W. McComb, G. K. Benedix, Why aqueous alteration in asteroids was isochemical: High porosity \neq high permeability. *Earth Planet. Sci. Lett.* **287**, 559–568 (2009). [doi:10.1016/j.epsl.2009.09.004](https://doi.org/10.1016/j.epsl.2009.09.004)
69. M. Y. Zolotov, An oceanic composition on early and today's Enceladus. *Geophys. Res. Lett.* **34**, L23203 (2007). [doi:10.1029/2007GL031234](https://doi.org/10.1029/2007GL031234)
70. D. R. Stegman, J. Freeman, D. A. May, Origin of ice diapirism, true polar wander, subsurface ocean, and tiger stripes of Enceladus driven by compositional convection. *Icarus* **202**, 669–680 (2009). [doi:10.1016/j.icarus.2009.03.017](https://doi.org/10.1016/j.icarus.2009.03.017)
71. R. V. Ackermann, R. W. Schlische, M. O. Withjack, The geometric and statistical evolution of normal fault systems: An experimental study of the effects of mechanical layer thickness on scaling laws. *J. Struct. Geol.* **23**, 1803–1819 (2001). [doi:10.1016/S0191-8141\(01\)00028-1](https://doi.org/10.1016/S0191-8141(01)00028-1)
72. D. Y. Wyrick, A. P. Morris, D. A. Ferrill, Normal fault growth in analog models and on Mars. *Icarus* **212**, 559–567 (2011). [doi:10.1016/j.icarus.2011.01.011](https://doi.org/10.1016/j.icarus.2011.01.011)
73. C. Spyropoulos, W. J. Griffith, C. H. Scholz, B. E. Shaw, Experimental evidence for different strain regimes of crack populations in a clay model. *Geophys. Res. Lett.* **26**, 1081–1084 (1999). [doi:10.1029/1999GL900175](https://doi.org/10.1029/1999GL900175)
74. D. W. Sims, D. Y. Wyrick, D. A. Ferrill, A. P. Morris, G. C. Collins, R. T. Pappalardo, S. L. Colton, Physical models of grooved terrain tectonics on Ganymede. *Geophys. Res. Lett.* **41**, 3774–3778 (2014). [doi:10.1002/2014GL060359](https://doi.org/10.1002/2014GL060359)
75. J. Fuller, J. Luan, E. Quataert, Resonance locking as the source of rapid tidal migration in the Jupiter and Saturn moon systems. *Mon. Not. R. Astron. Soc.* **458**, 3867–3879 (2016).
[doi:10.1093/mnras/stw609](https://doi.org/10.1093/mnras/stw609)
76. F. Tian, A. I. F. Stewart, O. B. Toon, K. W. Larsen, L. W. Esposito, Monte Carlo simulations of the water vapor plumes on Enceladus. *Icarus* **188**, 154–161 (2007).
[doi:10.1016/j.icarus.2006.11.010](https://doi.org/10.1016/j.icarus.2006.11.010)

77. N. H. Sleep, D. K. Bird, Niches of the pre-photosynthetic biosphere and geologic preservation of Earth's earliest ecology. *Geobiology* **5**, 101–117 (2007).
[doi:10.1111/j.1472-4669.2007.00105.x](https://doi.org/10.1111/j.1472-4669.2007.00105.x)
78. A. J. Brearley, R. H. Jones, in *Planetary Materials*, J. J. Papike, Ed. (Mineralogical Society of America, 1998), pp. 3-1–3-98.
79. J. P. Bradley, in *Meteorites, Comets, and Planets*, A. M. Davis, Ed. (Elsevier-Pergamon, 2003), pp. 689–713.
80. M. E. Zolensky, T. J. Zega, H. Yano, S. Wirick, A. J. Westphal, M. K. Weisberg, I. Weber, J. L. Warren, M. A. Velbel, A. Tsuchiyama, P. Tsou, A. Toppani, N. Tomioka, K. Tomeoka, N. Teslich, M. Taheri, J. Susini, R. Stroud, T. Stephan, F. J. Stadermann, C. J. Snead, S. B. Simon, A. Simionovici, T. H. See, F. Robert, F. J. M. Rietmeijer, W. Rao, M. C. Perronnet, D. A. Papanastassiou, K. Okudaira, K. Ohsumi, I. Ohnishi, K. Nakamura-Messenger, T. Nakamura, S. Mostefaoui, T. Mikouchi, A. Meibom, G. Matrajt, M. A. Marcus, H. Leroux, L. Lemelle, L. Le, A. Lanzirotti, F. Langenhorst, A. N. Krot, L. P. Keller, A. T. Kearsley, D. Joswiak, D. Jacob, H. Ishii, R. Harvey, K. Hagiya, L. Grossman, J. N. Grossman, G. A. Graham, M. Gounelle, P. Gillet, M. J. Genge, G. Flynn, T. Ferroir, S. Fallon, S. Fakra, D. S. Ebel, Z. R. Dai, P. Cordier, B. Clark, M. Chi, A. L. Butterworth, D. E. Brownlee, J. C. Bridges, S. Brennan, A. Brearley, J. P. Bradley, P. Bleuet, P. A. Bland, R. Bastien, Mineralogy and petrology of comet 81P/Wild 2 nucleus samples. *Science* **314**, 1735–1739 (2006).
[doi:10.1126/science.1135842](https://doi.org/10.1126/science.1135842) [Medline](#)
81. C. R. Glein, M. Y. Zolotov, E. L. Shock, The oxidation state of hydrothermal systems on early Enceladus. *Icarus* **197**, 157–163 (2008). [doi:10.1016/j.icarus.2008.03.021](https://doi.org/10.1016/j.icarus.2008.03.021)
82. T. M. McCollom, F. Klein, M. Robbins, B. Moskowicz, T. S. Berquó, N. Jöns, W. Bach, A. Templeton, Temperature trends for reaction rates, hydrogen generation, and partitioning of iron during experimental serpentinization of olivine. *Geochim. Cosmochim. Acta* **181**, 175–200 (2016). [doi:10.1016/j.gca.2016.03.002](https://doi.org/10.1016/j.gca.2016.03.002)
83. K. T. Howard, G. K. Benedix, P. A. Bland, G. Cressey, Modal mineralogy of CM2 chondrites by X-ray diffraction (PSD-XRD). Part 1: Total phyllosilicate abundance and the degree of aqueous alteration. *Geochim. Cosmochim. Acta* **73**, 4576–4589 (2009).
[doi:10.1016/j.gca.2009.04.038](https://doi.org/10.1016/j.gca.2009.04.038)
84. S. D. Vance, K. P. Hand, R. T. Pappalardo, Geophysical controls of chemical disequilibria in Europa. *Geophys. Res. Lett.* **43**, 4871–4879 (2016). [doi:10.1002/2016GL068547](https://doi.org/10.1002/2016GL068547)
85. M. Y. Zolotov, On the composition and differentiation of Ceres. *Icarus* **204**, 183–193 (2009).
[doi:10.1016/j.icarus.2009.06.011](https://doi.org/10.1016/j.icarus.2009.06.011)
86. U. Malamud, D. Prialnik, A 1-D evolutionary model for icy satellites, applied to Enceladus. *Icarus* **268**, 1–11 (2016). [doi:10.1016/j.icarus.2015.12.046](https://doi.org/10.1016/j.icarus.2015.12.046)

87. A. Neubeck, N. T. Duc, H. Hellevang, C. Oze, D. Bastviken, Z. Bacsik, N. G. Holm, Olivine alteration and H₂ production in carbonate-rich, low temperature aqueous environments. *Planet. Space Sci.* **96**, 51–61 (2014). [doi:10.1016/j.pss.2014.02.014](https://doi.org/10.1016/j.pss.2014.02.014)
88. T. Shibuya, M. Yoshizaki, M. Sato, K. Shimizu, K. Nakamura, S. Omori, K. Suzuki, K. Takai, H. Tsunakawa, S. Maruyama, Hydrogen-rich hydrothermal environments in the Hadean ocean inferred from serpentinization of komatiites at 300°C and 500 bar. *Prog. Earth Planet. Sci.* **2**, 46 (2015). [doi:10.1186/s40645-015-0076-z](https://doi.org/10.1186/s40645-015-0076-z)
89. G. Holland, B. Sherwood Lollar, L. Li, G. Lacrampe-Couloume, G. F. Slater, C. J. Ballentine, Deep fracture fluids isolated in the crust since the Precambrian era. *Nature* **497**, 357–360 (2013). [doi:10.1038/nature12127](https://doi.org/10.1038/nature12127) [Medline](#)
90. J. M. McDermott, J. S. Seewald, C. R. German, S. P. Sylva, Pathways for abiotic organic synthesis at submarine hydrothermal fields. *Proc. Natl. Acad. Sci. U.S.A.* **112**, 7668–7672 (2015). [doi:10.1073/pnas.1506295112](https://doi.org/10.1073/pnas.1506295112) [Medline](#)
91. A. J. Brearley, in *Meteorites and the Early Solar System II*, D. S. Lauretta, H. Y. McSween, Eds. (Univ. of Arizona Press, 2006), pp. 587–624.
92. J. Horita, M. E. Berndt, Abiogenic methane formation and isotopic fractionation under hydrothermal conditions. *Science* **285**, 1055–1057 (1999). [doi:10.1126/science.285.5430.1055](https://doi.org/10.1126/science.285.5430.1055) [Medline](#)
93. C. R. Glein, Noble gases, nitrogen, and methane from the deep interior to the atmosphere of Titan. *Icarus* **250**, 570–586 (2015). [doi:10.1016/j.icarus.2015.01.001](https://doi.org/10.1016/j.icarus.2015.01.001)
94. A. Bouquet, O. Mousis, J. H. Waite, S. Picaud, Possible evidence for a methane source in Enceladus' ocean. *Geophys. Res. Lett.* **42**, 1334–1339 (2015). [doi:10.1002/2014GL063013](https://doi.org/10.1002/2014GL063013)
95. T. M. McCollom, Abiotic methane formation during experimental serpentinization of olivine. *Proc. Natl. Acad. Sci. U.S.A.* **113**, 13965–13970 (2016). [doi:10.1073/pnas.1611843113](https://doi.org/10.1073/pnas.1611843113) [Medline](#)
96. E. L. Shock, H. C. Helgeson, D. A. Sverjensky, Calculation of the thermodynamic and transport properties of aqueous species at high pressures and temperatures: Standard partial molal properties of inorganic neutral species. *Geochim. Cosmochim. Acta* **53**, 2157–2183 (1989). [doi:10.1016/0016-7037\(89\)90341-4](https://doi.org/10.1016/0016-7037(89)90341-4)
97. E. L. Shock, H. C. Helgeson, Calculation of the thermodynamic and transport properties of aqueous species at high pressures and temperatures: Standard partial molal properties of organic species. *Geochim. Cosmochim. Acta* **54**, 915–945 (1990). [doi:10.1016/0016-7037\(90\)90429-O](https://doi.org/10.1016/0016-7037(90)90429-O)
98. A. P. Ingersoll, M. Nakajima, Controlled boiling on Enceladus. 2. Model of the liquid-filled cracks. *Icarus* **272**, 319–326 (2016). [doi:10.1016/j.icarus.2015.12.040](https://doi.org/10.1016/j.icarus.2015.12.040)

99. B. Jähne, G. Heinz, W. Dietrich, Measurement of the diffusion coefficients of sparingly soluble gases in water. *J. Geophys. Res.* **92**, 10767 (1987).
[doi:10.1029/JC092iC10p10767](https://doi.org/10.1029/JC092iC10p10767)
100. K. S. Johnson, Carbon dioxide hydration and dehydration kinetics in seawater. *Limnol. Oceanogr.* **27**, 849–855 (1982). [doi:10.4319/lo.1982.27.5.0849](https://doi.org/10.4319/lo.1982.27.5.0849)
101. G. M. Anderson, *Thermodynamics of Natural Systems* (Cambridge Univ. Press, 2005).
102. J. W. Johnson, E. H. Oelkers, H. C. Helgeson, SUPCRT92: A software package for calculating the standard molal thermodynamic properties of minerals, gases, aqueous species, and reactions from 1 to 5000 bar and 0 to 1000°C. *Comput. Geosci.* **18**, 899–947 (1992). [doi:10.1016/0098-3004\(92\)90029-Q](https://doi.org/10.1016/0098-3004(92)90029-Q)
103. J. W. Anthony, R. A. Bideaux, K. W. Bladh, M. C. Nichols, Eds., *Handbook of Mineralogy* (Mineralogical Society of America, 2015); www.handbookofmineralogy.org.